



Density functional methods applied to metalloenzymes

Timothy Lovell, Fahmi Himo, Wen-Ge Han, Louis Noodleman*

Department of Molecular Biology, TPC-15, The Scripps Research Institute, 10550 North Torrey Pines Road, La Jolla, CA 92037, USA

Received 2 July 2002; accepted 13 December 2002

Contents

Abstract	211
1. Introduction	212
2. Methods and modeling strategies	212
3. Manganese and iron-superoxide dismutases	214
4. Galactose oxidase	217
5. Glyoxalase I	219
6. Methane monooxygenase and ribonucleotide reductase	223
6.1 Methane monooxygenase	224
6.2 Ribonucleotide reductase	226
6.3 Interaction with the protein environment for structurally characterized MMOH and RNR clusters	227
6.4 MMOH(Q)	228
6.5 RNR(X)	229
6.6 Summary	230
7. Conclusions	230
Acknowledgements	231
References	231

Abstract

Density functional calculations for structures, spin states, redox energetics and reaction pathways are presented for some selected metalloenzymes. The specific enzymes examined are: (1) Fe and Mn superoxide dismutase for redox energetics and the role of second shell residues; (2) galactose oxidase (Cu enzyme) and (3) glyoxalase I (Zn enzyme) for reaction pathways, mechanisms, intermediates, and transition states (reaction barriers); (4) iron-oxo dimer enzymes methane monooxygenase and ribonucleotide reductase for characterizing the oxidized and reduced forms in terms of structures and protonation states, and for a proposed structure for the high-valent intermediate Q in MMO. The interaction of the active site with the surrounding protein environment is also explored in a number of cases either by using expanded quantum mechanically treated clusters, or by using electrostatic/dielectric representations of the protein–solvent environment.

© 2003 Elsevier Science B.V. All rights reserved.

Keywords: Density functional; Broken symmetry; Iron-oxo enzymes; Methane monooxygenase; Ribonucleotide reductase; Catalytic cycle; Redox; Poisson–Boltzmann; Electrostatics; Electron transfer; Proton transfer; H atom transfer; π -Cation interaction

Abbreviations: AF, antiferromagnetic; BP86, Becke88–Perdew86; B3LYP, Becke–Lee–Yang–Parr forms of exchange–correlation potentials; DFT, density functional theory; eT, electron transfer; ESP, electrostatic potential; F, ferromagnetic; GGA, generalized gradient correction; HS, high-spin; LS, low-spin; MEAD, macroscopic electrostatics with atomic detail; MMO, methane monooxygenase; pT, proton transfer; PW91, Perdew–Wang91; RNR, ribonucleotide reductase; SCRf, self-consistent-reaction-field; SOD, superoxide dismutase.

* Corresponding author. Fax: +1-858-784-8896.

E-mail address: lou@scripps.edu (L. Noodleman).

1. Introduction

Metalloenzymes catalyze many difficult reactions under mild conditions and with selectivity [1]. Examples include nitrogen fixation [2], hydrocarbon oxidation [3,4], generation of radicals for subsequent catalysis [5], and dismutation of superoxide (a radical anion) [6,7]. Of known proteins, about 40% contain metal ions based on analysis of the protein data bank (PDB). Very prominent among catalytic sites in metalloenzymes are the transition metals Fe, Zn, Mn, and Cu, in order of greatest to lesser frequency (based on a current analysis utilizing the metalloprotein data bank (MDB)) [8]. In this review, we will examine one (or more) metalloenzymes containing each of these metals.

The specific enzymes we will principally examine are: (1) Fe and Mn superoxide dismutases (Fe and MnSODs, mononuclear redox-active enzymes) [6,9]; (2) galactose oxidase (mononuclear Cu enzyme) [10]; (3) glyoxalase I (mononuclear Zn enzyme) [11]. (4) iron-oxo dimer enzymes (methane monooxygenase (MMO) and ribonucleotide reductase (RNR)) [12].

Catalytic reaction cycles typically involve making and breaking of bonds. Often, the transition metal active sites are redox active, and there can be coupling between electron transfer (eT) and proton transfer (pT) as well [13]. While in ‘pure’ eT metalloproteins, geometric reorganization is usually kept at a minimum to facilitate efficient eT, many redox active metalloenzymes undergo significant conformational changes at or near the active site [14]. Fe and Mn metalloenzymes (and related eT proteins) usually have high-spin (HS) metal sites in some or all steps of their catalytic cycles [13,15]. In dinuclear or polynuclear enzymes, these metal sites are often spin-coupled [16]. In other cases, as in Zn–Fe or Cu–Zn enzymes, bridging ligands link the metal sites electronically [17,18]. The positively charged metal ions and the negatively charged first shell ligands exhibit strong metal-ligand covalency, which can either tune the redox potential of the active site and/or shift the acidity of bound ligands [13,19]. In other non-redox cases, either some charge transfer to the metal (glyoxalase I, Zn), or spin coupling between a metal and a ligand radical (Cytosine in galactose oxidase) can initiate the catalytic cycle. Here the ligands are ‘noninnocent’, and can be radicals in some cases.

The next section provides some basic approaches for methods and modeling strategies.

2. Methods and modeling strategies

To treat metalloprotein active sites involving first row transition metals, we use density functional theory (DFT) methods with the generalized gradient approximation (GGA) (also called ‘nonlocal’ since it involves

terms in the gradient of the electron density) [20–22] or hybrid methods involving a linear combination of Hartree–Fock (HF) and DFT–GGA potentials [23,24]. Usually, we use spin-polarized methods which distinguish between α (spin-up) and β (spin-down) electron densities. The exchange–correlation potentials used in the next four sections are called the Becke88–Perdew86 (BP86) [20–22], the Perdew–Wang91 (PW91) [25], and the (B3LYP) (referring to work by Becke, Lee, Yang, and Parr on a hybrid type potential) [23,24]. For spin-coupled transition metal complexes like Fe-oxo dimer and FeS dinuclear and polynuclear systems, the method of broken-symmetry [26–30] allows one to characterize antiferromagnetically (AF) versus ferromagnetically (F) coupled systems. In systems that have net spin and/or are spin-coupled, there are additional spin degrees of freedom to consider, both from the spin-coupling and from examining whether the individual metal sites are HS, intermediate-spin (IS), or low-spin (LS). These issues are very well known from the behavior of spin-coupled systems and for spin-crossover and valence tautomeric systems; such phenomena are seen in many metalloenzymes, for example, comparing (LS) oxy-hemoglobin with (HS) deoxy-hemoglobin, or in oxy- versus deoxy-hemerythrin (Hr) (both are AF coupled but deoxy-Hr is very weakly coupled while oxy-Hr is more strongly coupled.) [31,32] In studying MMO intermediates and related synthetic systems, there are important correspondences among geometric structures, spin state structures, and energetics [33].

We have found partial or full geometry optimization to be essential in most cases not only for the active site structures themselves, but also for a consistent treatment of energetics since the ‘experimental geometry’ rarely gives the precise ‘theoretical’ minimum. (As we will discuss later, the ‘theoretical minima’ are not perfect and reflect both the structural model and the quantum methods used.) This is in agreement with the experience of other groups. Both first ligand shell and extended quantum models will be analyzed below.

The calculations begin with an initial protein structure derived from crystallography where possible, and then geometry and self-consistent-field (SCF) optimizations are performed. In addition to the usual limitations on the accuracy of protein crystal structures, there are other experimental problems to consider: (1) Redox heterogeneity—metalloenzymes are sometimes crystallized in a physical mixture of redox states; reduction may also be nonuniform through a crystal whether by chemical means, by partial oxidation, or by radiolytic reduction [15,34]; also the X-ray beam can be reducing for an initially ‘oxidized’ crystal. This happens quite often (but not exclusively) with strong synchrotron X-ray beams under cryogenic conditions where aquated electrons can reduce the metal sites, but is dependent also on the intrinsic redox potential of the active site, temperature,

and electron transport through the crystal. The oxidation state of the crystal can be tested by EPR methods before and after X-ray irradiation. (2) Proton heterogeneity—bound active site waters or amino acid residues like histidines or even aspartates or glutamates may be in a physical mixture of titration states [35,36]. Further, protonation states may differ with the metal oxidation state, and in various steps of the catalytic cycle. Both of these heterogeneities can have significant structural as well as energetic effects. (3) In addition to the resolution of the X-ray structure, it is important to consider that the active site structure obtained depends on the constraints in the structural model used by the particular research group. In the best work, metal-ligand bond length constraints are removed at the end of the refinement process so as to obtain an ‘unbiased’ structure. However, the quality of the result still depends on resolution. There are now a number of X-ray structures of very-high-resolution quality (about 1.6 Å or better), and many more metalloprotein structures of this quality should be available in the near future [37]. (4) There can be multiple conformers and/or fluxionality and then just taking an average crystallographic structure can give significant errors in geometries. (5) Typically, only some redox states and intermediates involved in a catalytic cycle have available X-ray structures; for the remaining intermediates and for all transition states, quantum calculations, strongly augmented by spectroscopic and related physical data and analysis are required to complete the picture for structures, energies, and properties. In some favorable cases, transition state analogues or analogues of intermediate states using bound inhibitors can be experimentally constructed. Then, it is valuable to evaluate these structurally and energetically for comparison with corresponding calculated intermediates and transition states.

The complete system can be divided into the ‘quantum cluster’ and ‘the environment’ [35,38,39]. For the ‘environment’ we employ dielectric and electrostatics approaches, with either direct geometric constraints on the location of the active site cluster or force field derived approaches for steric constraints. The electrostatic approach for the environment represents the solvent region as a dielectric medium with a high-dielectric constant ($\epsilon_s = 80$) and the protein as a low-dielectric medium ($\epsilon_p = 4$) containing also a partial charge representation of the protein derived from force field or solvation models in the literature [40–45]. From calculations on the gas phase quantum cluster, an electrostatic potential (ESP target potential) outside a van der Waals envelope around the cluster is computed, and best fit charges are determined which generate the closest ESP to the target potential in the least-squares sense. These charges are called ESP charges [46,47]. The three dielectric media ($\epsilon_s = 80$, $\epsilon_p = 4$, and $\epsilon_{\text{cluster}} = 1$)

and the protein partial charges are used along with the cluster based ESP charges to generate two potentials: (1) a protein field potential ϕ_{prot} acting in the cluster region and representing the dielectrically screened ESP due to the protein charges; (2) a reaction field potential ϕ_{react} representing the dielectric response of the three dielectric media to the quantum ESP charges. These electrostatic/dielectric energy calculations are implemented in the macroscopic electrostatics with atomic detail (MEAD) program package due to Bashford and his group to obtain the final equation for the sum of the reaction field and protein field energies E_{pr}

$$E_{\text{pr}} = 1/2 \sum q_i^{\text{ESP}} \phi(i)_{\text{react}} + \sum q_i^{\text{ESP}} \phi(i)_{\text{prot}}$$

The potentials ϕ_{react} and ϕ_{prot} are determined from the solution of the linearized Poisson–Boltzmann equation [41,48]. Ionic strength effects on the solvent region can also be included at the level of linearized Debye–Huckel theory. Similarly, a simple solvent medium surrounding the quantum cluster can be represented by a 2-dielectric model ($\epsilon_s = 80$, $\epsilon_{\text{cluster}} = 1$) for the solvent and cluster regions, respectively. Then there is only a reaction field term and the protein field term is absent. If a more detailed model for a cluster in solution is needed, a mixed quantum and continuum solvent model is often quite valuable with some discrete quantum water molecules and continuum solvent beyond [49]. Combinations of discrete quantum waters, discrete electrostatically described waters, and continuum dielectrics are also valuable for evaluating energetics of transition metal active sites embedded in proteins as shown in recent work on CuZn SOD [39].

The formulation given above is fairly rapid and simple, but this method does not allow for the change in the quantum cluster electronic structure and charge density in response to the dielectric media and the protein partial charges. This is the procedure followed for all the enzymes examined in detail in this review. However, we have also implemented the more complicated case where the potentials ϕ_{react} and ϕ_{prot} are incorporated back into the quantum DFT Hamiltonian forming a self-consistent-reaction-field (SCRf) method [38,49–51]. The SCRf procedure is likely to be advantageous in many cases since it allows for polarization of the quantum cluster in response to the ‘classical’ electrostatic/dielectric environment. However, in the protein region within SCRf, specifically quantum mechanical effects such as charge transfer (CT) between the quantum cluster and this environment are not allowed, nor is bond formation per se, or Pauli repulsion between atoms (the ‘quantum chemist’s steric interaction’). To incorporate these types of effects, the quantum cluster itself needs to be expanded. How to do this in an efficient manner is a significant issue, which we have undertaken based on a ‘building’ strategy (or an

‘accretion model’) [33,35]. The protein field potential and the associated protein field–quantum cluster interaction energy can be partitioned into a linear sum of terms from the different residues in the protein field region and further partitioned into sidechain residue versus mainchain peptide contributions. Analysis of these terms allows rank ordering of the energetic importance of different residues. The most energetically significant residues can then be switched into the ‘quantum region’ where a variety of contributing energy terms will contribute.

One further subtle point deserves mention. The ‘standard’ three dielectric model we often use has $\epsilon_p = 4$ for the entire protein region, which represents screening of protein and also cluster charges by the rest of the protein. However, at a charged and polar interface between the quantum cluster region and the protein region often found in metalloprotein active sites, strong charge–charge interactions can have large energies and lower mobility. Even with an electrostatic protein representation, it may then be a more accurate representation to expand the (low dielectric) $\epsilon = 1$ region to encompass the most strongly binding part of the protein region [39]. We have tried this ‘extended low dielectric’ model out on a number of problems with some success, particularly in very recent work on iron–sulfur systems. The other related point to remember is that when an ‘electrostatically described residue’ is switched into the quantum region, the dielectric for that residue is $\epsilon = 1$, as in the ‘extended low dielectric model’. In our current model, dynamic motion of the quantum region is usually not allowed, aside from state-to-state changes plus zero-point energy differences. This then forms a common model for comparison of the ‘extended quantum model’ with the ‘extended low dielectric model’ for the relevant residues. The interplay of protein dynamics with electrostatic screening versus the behavior of strongly charged or polar groups with limited mobility is a problem for considerable further study. We note also more complicated alternative ‘dual dielectric’ models have been proposed which distinguish between the response of the active site cluster to the protein field versus reaction field [52]. Alternatively, the protein dynamic response can be considered more explicitly using molecular dynamics methods, but this is outside the scope of the current discussion.

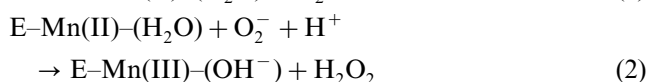
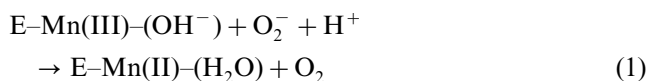
3. Manganese and iron-superoxide dismutases

Superoxide dismutases (SODs) are a diverse group of metalloenzymes critical to the existence of oxygen-tolerant organisms [53]. Their function is to dismutate two superoxides (radical anions) to molecular oxygen and hydrogen peroxide [6]. In combination with catalases which detoxify hydrogen peroxide (by converting

this to molecular oxygen plus water), SODs form an important part of biological defenses against toxic oxygen intermediates. This role applies to normal aerobic metabolism, to disease processes involving oxidative stress, and also to the metabolism of pathogenic bacteria (in their defense against free radical attack from the immune systems of higher organisms). MnSODs are found in the mitochondria of higher organisms (including human mitochondria), and related MnSODs and FeSODs are found in prokaryotes. Since mitochondria use over 90% of the cell’s oxygen, the mitochondrial electron transport chain produces a large quantity of oxygen radicals, and MnSOD is a primary biological defense against radical damage.

We have focussed on the comparative redox properties and associated catalytic cycles of MnSODs (including bacterial, human wild type, and the recently constructed human mutant enzymes), and on bacterial FeSOD. These results and conclusions are summarized in a very recent paper, Han et al. [54]. We discuss the most important conclusions below.

In MnSOD (and similarly in FeSOD), the overall catalytic dismutation proceeds via an alternating reduction of the Mn(III) enzyme (E–Mn(III)) and oxidation of the Mn(II) enzyme (E–Mn(II)), also called a Ping–Pong mechanism,



These two equations provide a global view of the overall catalytic cycle decomposed into two large steps. The first step represents binding and then inner sphere eT by superoxide $\text{O}_2 \rightarrow \text{O}_2^- + 1\text{e}^-$ to the active site, and the related redox energy for the enzyme active site, $\text{E–Mn(III)–(OH}^-) + 1\text{e}^- + \text{H}^+ \rightarrow \text{E–Mn(II)–(H}_2\text{O)}$ (called ‘the coupled redox potential’), the sum of these two reactions giving Eq.(1). Since the $\text{O}_2^- \rightarrow \text{O}_2$ redox potential is well-established, the coupled redox potential is the important unknown. In Eq.(2), the binding and reduction of the second superoxide to protonated peroxide occurs. The Mn coordination changes from 5-to-6-to-5 in both halves (Eq.(1) and Eq.(2)) of the reaction cycle [6]. There are two pTs to the peroxide, one internal to the active site from the coordinated H_2O , and one from a proton donor external to the active site. Further, since this is a catalytic cycle, the net reaction is just $2\text{O}_2^- + 2\text{H}^+ \rightarrow \text{O}_2 + \text{H}_2\text{O}_2$ (this energy is again well-known) which is just the sum of Eq.(1)Eq.(2). The redox potential must be matched to somewhere near the middle of the range for the respective standard redox potentials for O_2/O_2^- and for $\text{O}_2^-/\text{H}_2\text{O}_2$, that is, somewhere between -0.16 V (for unit activity of O_2) and $+0.89$ V for H_2O_2 at pH 7. This is a rough estimate of the

range, since the law of mass action under cellular conditions of O_2 , O_2^- , H_2O_2 and protons dictates the driving force for the different steps under steady state or transient conditions.

There are two important implications here, one experimental and one theoretical/computational. The critical experimental implication is that kinetic rate constants linking intermediates for either Eq.(1) or Eq.(2) are sufficient to experimentally evaluate the coupled redox potential, which is difficult to obtain by more direct redox measurements (using electrochemistry with redox mediators). Since sufficient kinetic data has been measured for Eq.(2) (but not for Eq.(1)), we used this information to evaluate the coupled redox potential from the kinetic rate constants alone. This allows the experimental redox potentials of bacterial MnSOD from *Thermus thermophilus* to be compared with those from human wild type and the human mutant enzyme Glutamine143→Asparagine for the first time. Computationally, we have evaluated the redox potentials for these three MnSOD enzymes, and also for the *Escherichia coli* MnSOD and *E. coli* FeSOD. While the calculated absolute redox potentials deviate significantly from experiment, the predicted relative redox potentials determined by our combined density functional/electrostatics methods agree very well with those observed from reaction kinetics for MnSOD from *T. thermophilus*, human wild type, and human Gln143/Asn. The last is expected (and now observed via reaction kinetics analysis) to have a very high redox potential since the reduced species is dominant in the X-ray crystal structure, unlike *T. thermophilus* and human wild type MnSOD, which are evidently mixtures of oxidized and reduced states in the X-ray structures.

There are four relevant redox and protonation states for MnSOD (similarly, also for the FeSOD enzyme): $Mn(III)(OH^-)$, $Mn(III)(H_2O)$, $Mn(II)(OH^-)$,

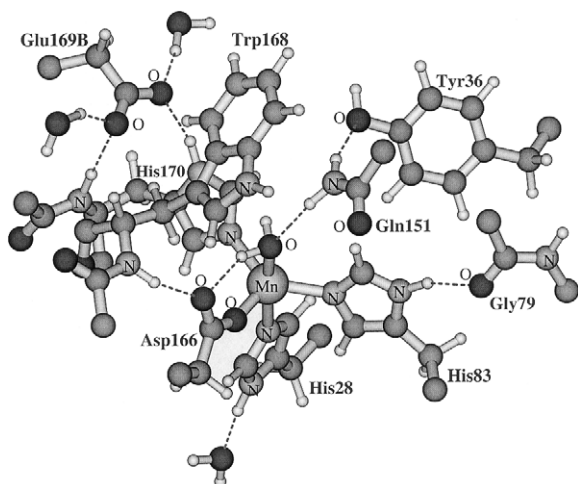


Fig. 1. The active site of Mn(Fe)SOD. Labels are taken from MnSOD of *T. thermophilus*.

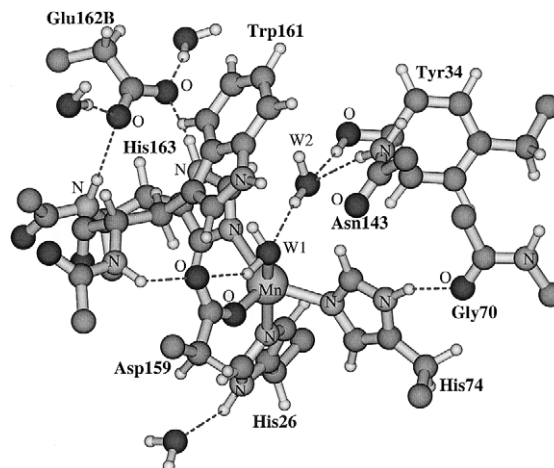


Fig. 2. The active site of mutant Q143N human MnSOD. After the replacement of Gln143→Asn in Q143N, an extra water molecule (labeled as W2) appears in the active site and is H-bonded with the original H_2O or OH^- ligand (W1) and both Tyr34 and Asn143 side chains.

$Mn(II)(H_2O)$, of which $Mn(III)(OH^-)$, $Mn(II)(H_2O)$ are by far the most energetically stable intermediates. We have evaluated the energies and structures of all of these for very large quantum cluster models (including over 100 atoms in the active site) of all the enzymes cited above. Fig. 1 depicts the active site and contains all the residue side chains and backbone in our large model. In addition, we have included the Trp ring (Trp 168) which is not in our current largest model. (More discussion of this will be given later.) Our computational analysis supports the assessment of the experimental kinetics of Silverman et al. [55–57], showing that the probable pT pathway proceeds from Tyr to Gln to the Mn bound hydroxyl (here depicted as water). The shorter Asn side chain allows for an additional water between Asn and the metal-bound-water (or hydroxyl). See Fig. 2 where the altered H-bonding network into the active site is depicted.

The observed redox shift relative to the *T. thermophilus* enzyme redox potential determined from our analysis of experimental reaction kinetics is -0.09 V for human wild type versus $+0.18$ V for the Q143N mutant of human MnSOD. By comparison, the calculated redox shifts by combined DFT/electrostatics methods is -0.04 versus $+0.14$ V for human WT versus Q143N, giving very good agreement in redox trends between the kinetics analysis and the DFT/electrostatics methodology. From a comparison of Figs. 1 and 2, and from more detailed structural analysis in Han et al. [54] the additional water in the Asn mutant provides more stability to the reduced $Mn(II)H_2O$ state than to the oxidized $Mn(III)(OH^-)$ compared with Gln. It appears that the water W2 hydrogen bonds (via its protons) more effectively to the Mn bound water W1 than the Gln side chain NH_2 does. From the energetic analysis of

the DFT/electrostatics, a larger change occurs upon $\text{Mn(III)H}_2\text{O} + 1e^- \rightarrow \text{Mn(II)H}_2\text{O}$ reduction rather than in the ‘earlier’ $\text{Mn(III)(OH}^-) + 1\text{H}^+ \rightarrow \text{Mn(III)H}_2\text{O}$ step. This is ‘Born–Haber’ cycle analysis, and does not necessarily represent the actual reaction path. An equivalent set of steps in the thermochemical cycle is to consider first $\text{Mn(III)(OH}^-) + 1e^- \rightarrow \text{Mn(II)(OH}^-)$ and second $\text{Mn(II)(OH}^-) + 1\text{H}^+ \rightarrow \text{Mn(II)H}_2\text{O}$. Here the Asn mutant has a much more positive redox potential (step 1) than the native Gln enzyme, while the protonation process (step 2) has a much lower free energy for the native Gln than in the Asn mutant. In Eq.(1), our DFT/electrostatics and the kinetic analysis support a gated eT process where the pT reaction occurs prior to or concerted with the eT from the O_2^- to the Mn(III)(Fe(III))SOD center. A lack of available protons can be rate limiting either in the first half or in the second half of the reaction cycle (Eqs.1,2).

While the trend in redox shifts between the *T. thermophilus* bacterial enzyme, and the native human versus Gln/Asn mutant is well-predicted by the DFT/electrostatics method, the predicted absolute redox potential for MnSOD differs substantially from that obtained experimentally. The absolute *T. thermophilus* MnSOD redox potential from reaction kinetics analysis is +0.40 V versus a standard hydrogen electrode (as extrapolated to pH 7) while the corresponding DFT/electrostatics predicted value is –0.25 V, an error of about +0.65 V. By contrast, use of the same DFT methodology for *E. coli* FeSOD gives a calculated redox potential of +0.16 versus +0.25 V (extrapolated to pH 7) from spectroelectrochemical redox measurements, +0.22 V at pH 7.4.

Part of the larger error for MnSOD can be traced by comparison with the analogous behavior of $\text{Mn}^{2+,3+}$ ions in aqueous solution, and by contrast with $\text{Fe}^{2+,3+}$ (aqueous) [49]. (The calculations involved two discrete water shells with six and twelve 1st and 2nd shell waters, and continuum solvent beyond with SCRF. This is fairly analogous in size and shape to the active site clusters for MnSOD and FeSOD that we have used, and with the Poisson–Boltzmann electrostatic model for the remaining protein–solvent.) Near neutral pH, both Mn^{3+} and Fe^{3+} in aqueous solution contain one bound (OH^-), so that the first coordination shell is $\text{M}^{3+}(\text{H}_2\text{O})_5(\text{OH}^-)$ ($\text{M} = \text{Mn, Fe}$). The one-electron reduction to M^{2+} is, therefore, analogous to the coupled redox process in the MSOD systems since $\text{M}^{3+}(\text{H}_2\text{O})_5(\text{OH}^-) + 1e^- + 1\text{H}^+ = \text{M}^{2+}(\text{H}_2\text{O})_6$ with both reactants and products solvated by further water shells. One way to break up this reaction is to consider the protonation of the M^{3+} complex first and then the $1e^-$ reduction of $\text{M}^{3+}(\text{H}_2\text{O})_6$ second. For Mn, the protonation step ($\text{Mn}^{3+}(\text{aq})$ is too strongly acidic) has a large error with the DFT exchange–correlation potential (BP86) we used, while the error in the $1e^-$ reduction step is negligible. By

contrast, for Fe, the protonation step has a very similar error to Mn, but the $1e^-$ redox step has a nearly compensating error. It is then not surprising that the coupled redox process $\text{Mn}^{3+}(\text{OH}^-)(\text{aq}) \rightarrow \text{Mn}^{2+}(\text{aq})$ contains a large error (0.36 V), while the corresponding error for $\text{Fe}^{3+}(\text{OH}^-)(\text{aq}) \rightarrow \text{Fe}^{2+}(\text{aq})$ is only 0.07 V. This systematic error in BP86 alone accounts for about half of the observed +0.65 V error in MnSOD redox potential and nearly all the small error for FeSOD. What then accounts for the remaining error in the calculated MnSOD redox potential?

We have noted that the relevant Trp sidechain (Trp161 in human mitochondrial MnSOD, Trp 168 in *T. thermophilus* MnSOD) is missing from our current quantum models clusters, although it was included in the electrostatic protein representation. (ESP point charges on atom centers miss the quadrupole moment due to the π system, see below.) Further, simple charge accounting shows that the active site of MnSOD is positively (+1) charged in either of the two most stable redox states $\text{Mn(III)(OH}^-)$ and $\text{Mn(II)(H}_2\text{O)}$. In Figs. 1 and 2, if Glu169B (or Glu162B) are excluded, the remaining cluster has charge +1, concentrated on the Mn ion and the bound H_2O , with the $\text{Mn(II)(H}_2\text{O)}$ unit more positively charged than the $\text{Mn(III)(OH}^-)$ unit based on ESP analysis (see Li et al., 1999, Table 8) [35] and the positive charge more concentrated toward the indole ring of Trp. π -cation interactions are known to be strong and stabilizing when a Trp π system interacts with a cationic center nearby. This interaction is of charge–quadrupole type and thus drops off roughly as $1/r^3$ (Note that Glu169B lies beyond Trp168 when viewed from $\text{Mn(H}_2\text{O)}$). In recent work, Zaric and coworkers have examined this π -cation interaction for the azide inhibited form of FeSOD [58]. In the presence of the metal-bound azide anion the active site has $\text{Fe(III)(H}_2\text{O)}$ form [6,35,59] While they did not evaluate the redox potential, Zaric et al. used DFT calculations (B3LYP with Gaussian98) on an active site model to determine the indole Trp interaction energy with the active site complex as 10 kcal mol^{–1}. It is then quite likely that inclusion of the Trp indole ring will significantly shift the calculated redox potentials of FeSOD and MnSOD positively. At the same time, the current calculated acidities of bound H_2O in the oxidized Fe(III)SOD and Mn(III)SOD are very high (very negative $\text{p}K_a$ values) [35,54], and these calculated acidities are expected to be diminished (positive $\text{p}K_a$ shifts) when Trp is incorporated in the quantum model via the same π -cation interaction. This is an important problem for future work.

In our earlier work [35], simpler quantum active site models than shown in Figs. 1 and 2 were explored using the accretion model. We concluded that the two most important second shell residues contributing significant positive shifts to the coupled redox potential are

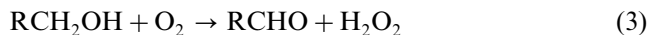
Glu169B and Gln151 in *T. thermophilus*. These redox shifts are obtained by shifting the residue from the electrostatic description (in the protein region with $\epsilon = 4$) into the quantum active site cluster. (However, for Gln151, the gas phase H-bonding acting alone favors Mn(III)(OH⁻), implying a negative shift; this result is more consistent with Miller's observations, see below).

In very recent work, Miller and coworkers [60] have examined the 'hydrogen-bond-mediated tuning' of the redox potential in native *E. coli* FeSOD versus Fe substituted into native *E. coli* MnSOD. The redox potential for native *E. coli* FeSOD is several hundred millivolts more positive than in the Fe-substituted MnSOD. DFT calculations (ADF 2000 with BP86) indicate that the likely source of this difference is the different position of the Gln side chain. The much closer Gln side chain as in MnSOD and the Fe-substituted MnSOD destabilizes the Fe(II)H₂O compared with Fe(III)(OH⁻) accounting at least qualitatively for the higher redox potential in native *E. coli* FeSOD.

These DFT results look promising both for assessment of redox and protonation processes, and for the more difficult analysis of the entire catalytic cycle. Higher resolution X-ray structures for important intermediates, mutant structures, and inhibitor bound complexes would be very helpful, along with experimental tools to determine detailed redox and protonation states.

4. Galactose oxidase

Galactose oxidase (GO) belongs to the rapidly growing family of radical enzymes [10,61]. It is a mononuclear type 2 copper enzyme that catalyzes the two-electron oxidation of a large number of primary alcohols to their corresponding aldehydes, coupled with the reduction of dioxygen to hydrogen peroxide:



The protein is a single polypeptide with molecular mass of ca. 68 kDa. To perform the two-electron chemistry, the enzyme utilizes, in addition to the copper center, a protein radical cofactor, which has been assigned to the Tyr272 residue. GO can exist in three distinct oxidation states: the highest state with Cu(II) and tyrosyl radical, the intermediate state with Cu(II) and tyrosine, and the lowest state with Cu(I) and tyrosine. The highest oxidation state is the catalytically active one. The protein radical couples AF with the copper ion, resulting in an EPR silent species.

The X-ray crystal structure of the active form of GO has been determined at pH 4.5 and 7.0 [62]. The copper site was found to be close to the surface with essentially square-pyramidal coordination with Tyr495 in axial position and Tyr272, His581, His496 and a water or

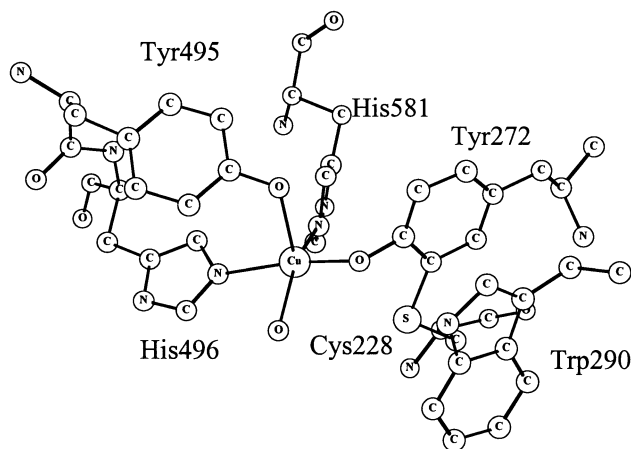
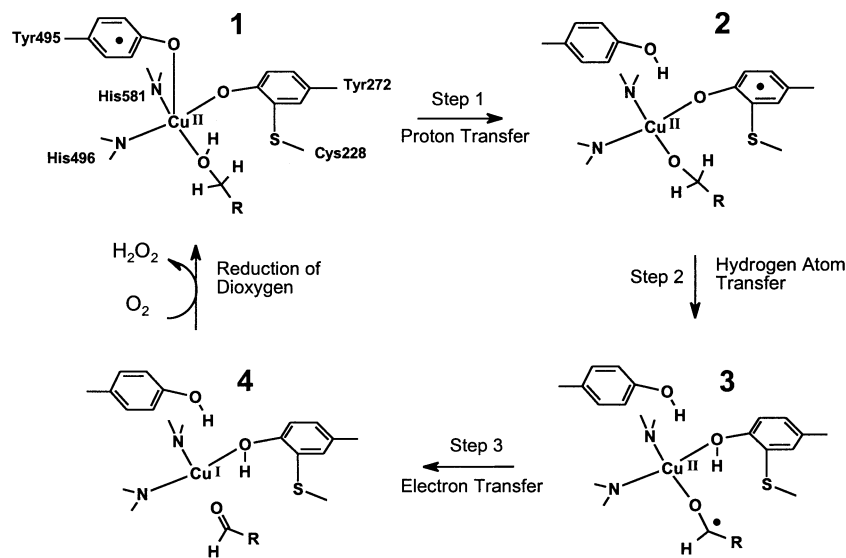


Fig. 3. Crystal structure of the active site of galactose oxidase. The substrate replaces the exogenous water in the equatorial position.

acetate to be replaced by substrate in equatorial positions (Fig. 3). Furthermore, the Tyr272 residue was found to be cross-linked to a cysteine residue (Cys228) through a thioether bond at the *ortho*-position to the phenol OH. The Tyr–Cys moiety is π -stacked to a tryptophan residue (Trp290), which also controls entry to the active site. Another interesting feature of the active site is the direct backbone link between the consecutive amino acids Tyr495 in axial position and His496 in equatorial position.

The proposed catalytic mechanism for GO is shown in Scheme 1 [63]. After the substrate binds to the equatorial copper position (occupied by water or acetate in the crystal structures), the first step is a pT from the alcohol to the axial tyrosinate (Tyr495). Next, a hydrogen atom is transferred from the substrate to the modified tyrosyl radical. The resulting substrate-derived ketyl radical is then oxidized through eT to the copper center yielding Cu(I) and aldehyde product. The two latter steps have been suggested to occur simultaneously in a concerted manner [64]. The Cu(I) and tyrosine are, finally, reoxidized by molecular oxygen, regenerating Cu(II) and tyrosyl, and giving hydrogen peroxide as product.

In the calculations [65], the two histidines were modeled using imidazoles, the equatorial tyrosine using SH-substituted phenol, whereas the somewhat smaller, but fully adequate, vinyl alcohol served as model for the axial tyrosine. The simplest alcohol, methanol, was used as a substrate. The rest of the phenol ring of the axial tyrosine and the backbone link between it and the equatorial histidine (His496) were included as molecular mechanics atoms, using the integrated molecular orbital/molecular mechanics (IMOMM) hybrid method [66]. This method uses quantum mechanics and molecular mechanics descriptions for different parts of the system, and it has proven to be successful in the quantification of steric effects in a number of organometallic applica-



Scheme 1. Proposed reaction mechanism for galactose oxidase.

tions. A charge-neutral model was used for galactose oxidase, which implies that one of the histidine ligands needs to be deprotonated in order to obtain the correct oxidation state of the copper atom.

It was found that the first step, the pT from the substrate to Tyr495 (step 1 in Scheme 1), occurs with a very low barrier (less than 3 kcal mol⁻¹). The exothermicity was calculated to be 3.2 kcal mol⁻¹. At this point, one important result that came out from the calculations was that the radical site prior to the pT (1 in Scheme 1) is not the equatorial cysteine-substituted tyrosine residue, but rather the axial tyrosine. The axial position is the weakest one in the square-pyramidal coordination of Cu(II), and thus the most natural place for the radical to be in. This is contrary to the accepted picture for the enzyme, but not in conflict with any experiment. In fact, model complexes experiments [67] show that the radical is most likely located axially in the non-square-planar coordination of the copper. Also Car–Parrinello calculations by Rothlisberger and Carloni [68] on these model systems confirm this fact.

After the pT, the radical is located at the equatorial tyrosine, implying that simultaneously with the pT an electron is moved from the equatorial tyrosine to the axial one.

The second step in the proposed mechanism of GO is a hydrogen atom transfer from the substrate to Tyr272 radical (step 2 in Scheme 1). On the basis of isotope substitution experiments, this step has been shown to be at least partially rate-limiting and probably the major rate-limiting step. Fig. 4(A) shows the optimized structure for the transition state of this hydrogen atom transfer. The barrier was calculated to be 13.6 kcal mol⁻¹. It is known that turnover rates of alcohols exhibit strong substituent effect [64b]. For instance, galactose has a turnover number of 800 s⁻¹, while

ethanol has a number of 0.02 s⁻¹ [69]. Assuming the hydrogen atom to be fully rate-determining, a barrier of ca. 14 kcal mol⁻¹ can be estimated using the kinetic data for galactose as substrate [4]. For ethanol, the barrier can be estimated to be ca. 6 kcal mol⁻¹ higher than for galactose. Although the DFT-calculated barrier (for methanol) is somewhat lower than the experimental estimation, it does indeed provide strong support for the proposed mechanism.

As seen in Fig. 4(A), the critical C–H bond has stretched to 1.36 Å at the transition state, and the H–O bond to 1.24 Å. At the transition state, one spin is located at the copper ($s = 0.49$) and the other is shared between the tyrosine ($s = 0.15$) and the substrate ($s = 0.49$). Consistently with the tyrosyl radical being a π -radical, we note that the hydrogen atom is transferred perpendicularly to the phenol ring plane. Stretching the phenol O–H bond in the plane of the ring would lead to a high-energy σ -radical.

The hydrogen atom transfer is proposed to result in a substrate derived ketyl radical (structure 3 in Scheme 1), which then would be oxidized through eT to the copper center, yielding Cu(I) and the aldehyde product (structure 4 in Scheme 1). By moving from the transition state structure towards the product, this proposed radical intermediate was localized (Fig. 4(B)). The energy of the intermediate is 4.9 kcal mol⁻¹ down from the transition state, making the hydrogen atom transfer step endothermic by 8.7 kcal mol⁻¹.

The intermediate is very unstable, with the barrier for its collapse to the closed shell Cu(I) and aldehyde product being very small. In practice, this radical intermediate is, therefore, probably impossible to detect.

The ketyl radical intermediate will readily reduce the copper center, yielding Cu(I) and aldehyde. The eT step was from the calculations estimated to be exothermic by

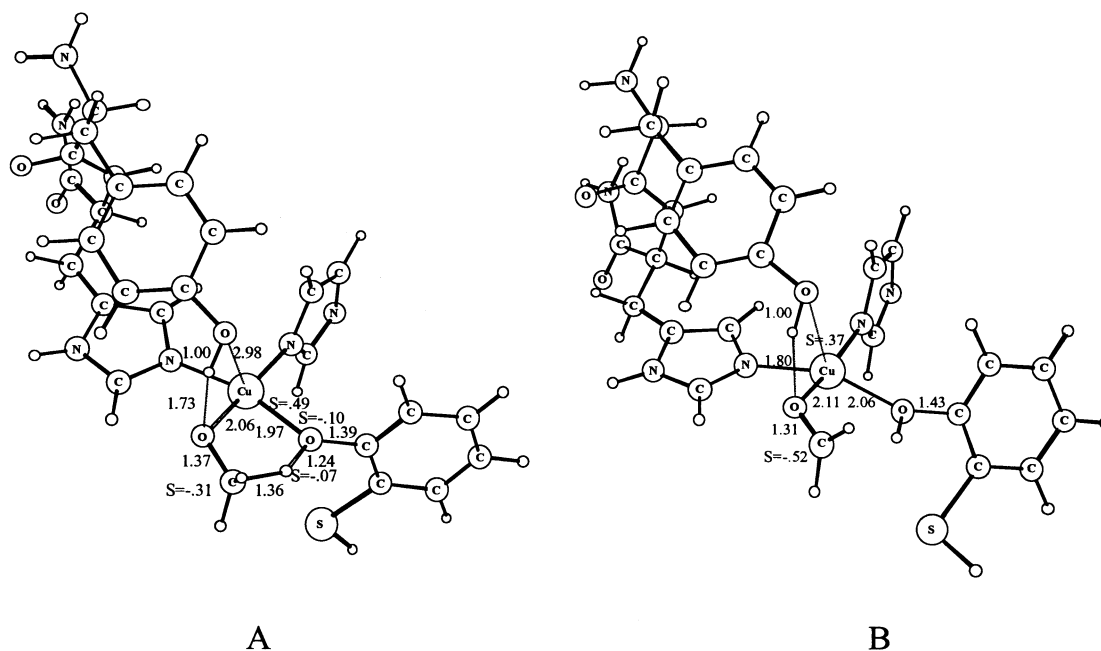


Fig. 4. Optimized geometries of (A) the transition state for the proposed rate-limiting hydrogen atom transfer and (B) the ketyl radical intermediate (structure **3** in Scheme 1).

ca. 5 kcal mol^{-1} . Energy is instead gained through the binding and one-electron reduction of dioxygen. Assuming the aldehyde product is released at this stage, and that dioxygen occupies its coordination position, O_2^- is calculated to bind to copper by $20.6 \text{ kcal mol}^{-1}$ more than the substrate alcoholate ($^- \text{OCH}_3$). The calculated potential energy curve for the steps discussed above is displayed in Fig. 5.

Finally, a few words about the role of the tyrosine–cysteine cross-link. It has been suggested that this thioether bond is in part responsible for the $0.5\text{--}0.6 \text{ V}$ lowering of the oxidation potential of this species compared with normal tyrosine [70]. Running the

calculations with and without the sulfur substitution, gave essentially the same potential energy curve, within $\pm 1 \text{ kcal mol}^{-1}$, indicating that the cross-link has small electronic effect on the catalysis. Its function is probably mainly structural.

5. Glyoxalase I

Glyoxalase I (GlxI) is a part of the glyoxalase system, which catalyzes the glutathione-dependent conversion of toxic methylglyoxal to D-lactate [11,71]. GlxI converts hemithioacetal (formed from methylglyoxal and glu-

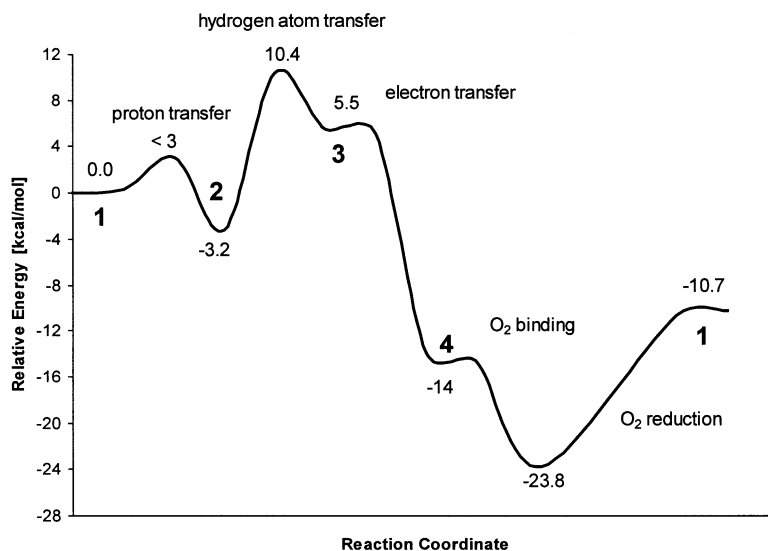
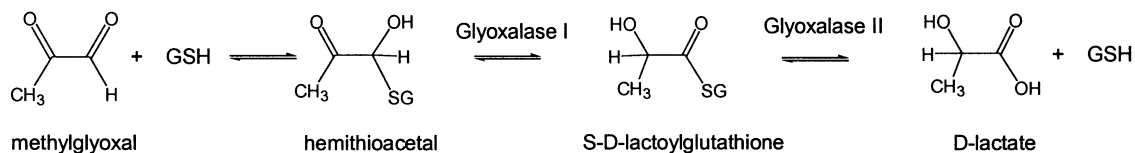


Fig. 5. Calculated potential energy surface for the mechanism of galactose oxidase.



Scheme 2. Reactions catalyzed by the glyoxalase system.

tathione) to *S*-D-lactoylglutathione, while glyoxalase II (GlxII) takes the latter as a substrate and converts it to *D*-lactate and glutathione (Scheme 2). The glyoxalase system has been suggested as a target for anti-cancer and anti-malarial drugs, as an increase in methylglyoxal can produce toxic effects by reacting with RNA, DNA and proteins [72].

Human GlxI is a homodimer of 43 kDa and requires Zn^{2+} for its catalytic function, showing however, significant catalytic activity with other divalent ions, like Mg^{2+} , Co^{2+} , Mn^{2+} , Ni^{2+} , and Ca^{2+} [73]. Human GlxI has been crystallized in complex with several inhibitors, out of which the most interesting structure is the one with *S*-(*N*-hydroxy-*N*-*p*-iodophenylcarbamoyl)glutathione (HIPC–GSH) [74]. This is a transition state analogue that mimics the enediolate intermediate believed to be formed in the reaction of GlxI. The substrate analogue was found to be bound directly to the Zn by its carbamoyl oxygens in a *cis*-conformation (Fig. 6), which shows that the reactions take place in the first ligation shell.

The catalytic reaction of GlxI is generally accepted to proceed via an enolate intermediate, resulting from a base abstracting a proton from the substrate. Based on the HIPC–GSH crystal structure and mutagenesis

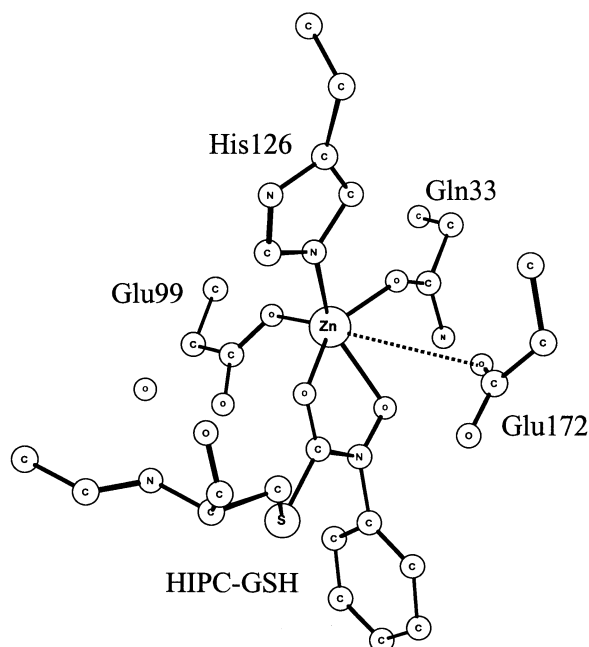


Fig. 6. Crystal structure of the active site of glyoxalase in complex with the HIPC–GSH inhibitor.

experiments, this base was proposed to be the Zn-ligand Glu172. In the HIPC–GSH structure, Glu172 was interestingly found to be displaced from the Zn (Zn–O distance 3.3 Å) as compared with the other structures. It was suggested that the displacement of this residue from the Zn upon substrate binding results in a $\text{p}K_{\text{a}}$ shift of the carboxylate group to more match the substrate $\text{p}K_{\text{a}}$, which is lowered by the Zn interaction. Not much is known about the steps after the initial pT. In particular, it is unclear whether other residues are involved in the catalytic process or whether the Glu172 residue alone performs all the pT steps necessary for the reaction.

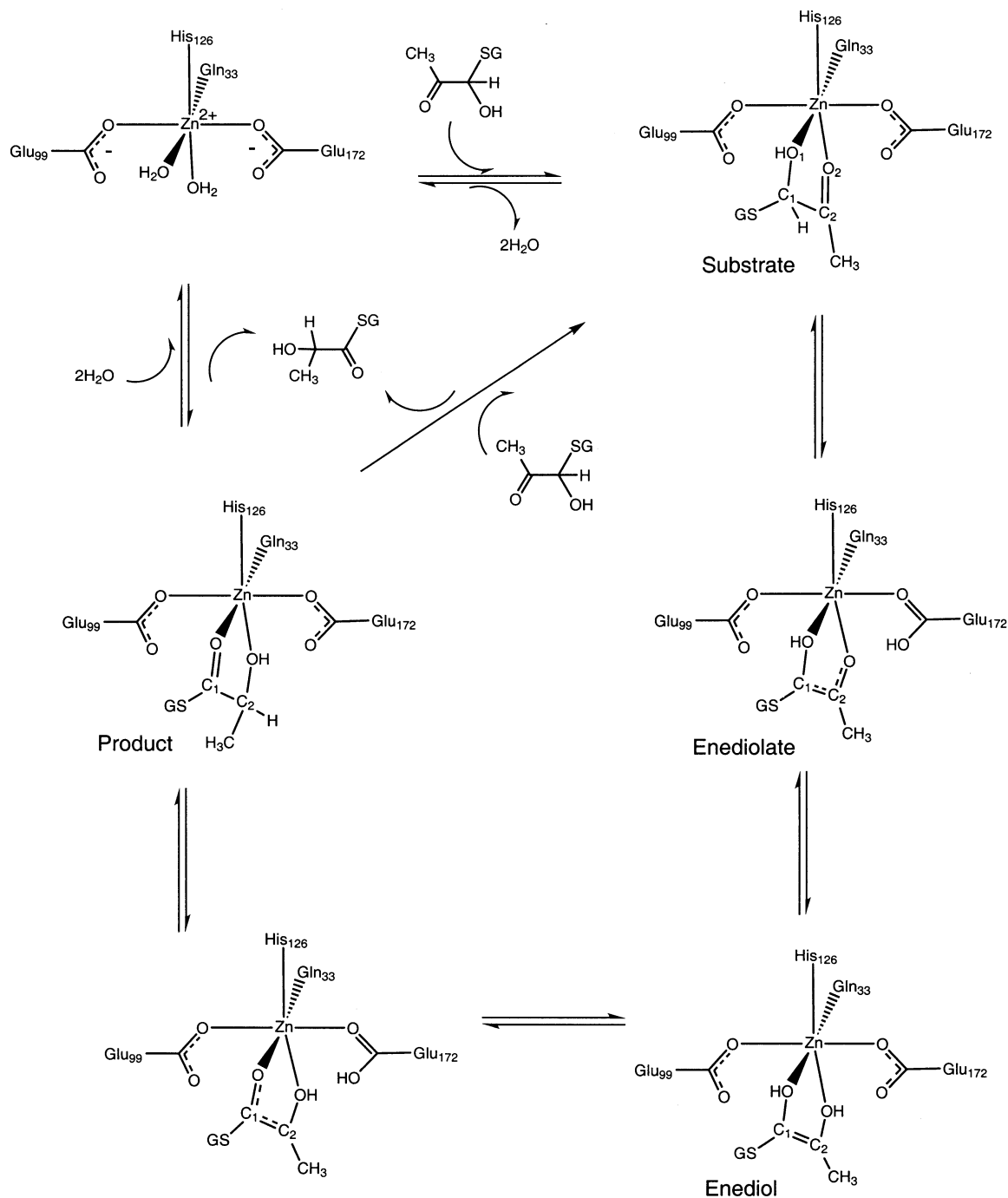
One of the remarkable features of GlxI is that it can process both the *S*- and *R*-diastereomers of the substrate, with nearly equal efficiencies [75]. Both substrates give the same chirally deuterated product, indicating stereospecific proton delivery.

The full catalytic mechanism of GlxI was investigated using the hybrid DFT functional B3LYP [76]. In the calculations, only the first ligation shell of the Zn was included. The Zn ligands were modeled as follows: histidine by imidazole, glutamates by formates, and glutamine by formamide. The hemithioacetal substrate was truncated at the sulfur of the glutathione (see Fig. 6).

The first step in the catalytic mechanism of GlxI is proposed to be a pT from substrate C1 to Glu172. Fig. 7 shows the optimized transition state structure (TS1) for this reaction (A) and the resulting enediolate intermediate (B). The calculated barrier is 14.4 kcal mol⁻¹, in excellent agreement with the known reaction rate ($k_{\text{cat}} = 1500 \text{ s}^{-1}$, corresponding to an activation barrier of ca. 14 kcal mol⁻¹). The critical C–H distance at TS1 is 1.47 Å and the H–O distance is 1.17 Å. From these results, it can be concluded that Glu172 is perfectly able to effect the initial proton abstraction step without the need to displace it from the Zn. The Zn-ligation is apparently sufficient to reduce the $\text{p}K_{\text{a}}$ of the substrate and make the pT feasible.

Upon pT, the substrate forms an enediolate intermediate. This intermediate was found to be quite high in energy, 12.6 kcal mol⁻¹ higher than the reactant, and only 1.8 kcal mol⁻¹ down from TS1.

In going from hemithioacetal substrate to the enolate intermediate (Fig. 7B), via TS1 (Fig. 7A), it is informative to look at some geometrical changes that reflect the chemistry of this step. The substrate C1–C2 single bond is shortened from 1.54 to 1.39 Å (1.43 Å at TS1) and the



Scheme 3. Proposed reaction mechanism for glyoxalase I.

that GlxI is nonstereospecific with respect to the proton abstraction, but it is stereospecific with respect to the proton delivery to the enediol intermediate [75]. Based on the pseudo *C*₂ symmetry of the active site, Cameron et al. suggested that Glu99 can abstract the proton from the *R*-enantiomer [74]. The fact that this residue was not displaced from the Zn upon substrate binding (as is the case for Glu172) was believed to speak against this. However, from the results of the calculations discussed above, we know that this displacement is not needed to

perform the initial proton abstraction. The calculations show that the transition state for the pT from C1 to Glu99 in the case of the *R*-enantiomer of the substrate has just slightly higher value than the *S*-substrate, ca. 2 kcal mol⁻¹. The transition state structures are very similar. The structures and energies of the enediolate intermediates are also, due to the high symmetry of the active site, very similar. Of course, the symmetry between Glu172 and Glu99 is idealized in the small model used in the active site. In the actual enzyme, there

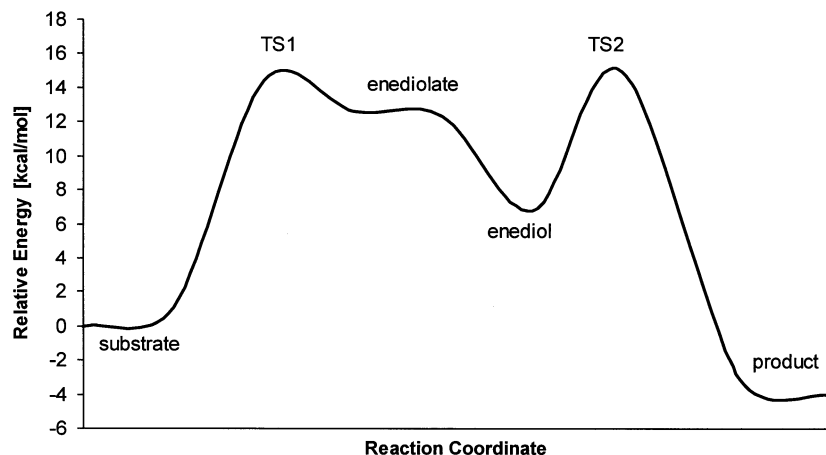


Fig. 9. Calculated potential energy surface for the mechanism of glyoxalase I.

could be some energetic or structural differences between the *S*- and *R*-reactions for the initial pT step. The results of the calculations show, however, that the basic features are the same.

So, up to this point, the *S*- and *R*-reactions are symmetric. The subsequent steps must deviate from the symmetry though. A fully analogous mechanism to that of Scheme 3, in which Glu99 also effects the second pT from O1 to C2, would yield the incorrect L-form of the product. To obtain the D-lactoylglutathione product, Glu172 was proposed to affect the transfer of the second proton, as in the case of the *S*-reactions. The transition state for this is the same as TS2 of the *S*-mechanism (Fig. 8). This way, the correct enantiomer of the product is produced.

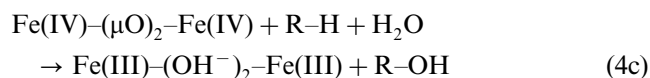
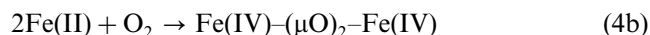
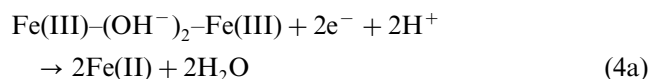
Although the individual reaction steps are identical to the *S*-mechanism, the *R*-reaction mechanism differs in a very important point. The difference is that the *R*-reactions involve two bases (Glu99 and Glu172) as opposed to only one base in the *S*-case (Glu172). It is currently not understood why the two mechanisms should diverge and break the symmetry. This result is ultimately dictated by the fact that both the *S*- and the *R*-enantiomers of the substrate yield the same form of the product [75]. The symmetry has to be broken to satisfy this condition.

6. Methane monooxygenase and ribonucleotide reductase

Iron-oxo dimer enzymes carry out a broad range of important and chemically difficult reactions in biological systems [3,77]. In this review, our main focus will be on the catalytically active hydroxylase enzyme of soluble MMO and on Class I RNR. Among the members of the binuclear non-heme iron family, MMO and RNR show extensive similarity with both displaying the Glu/Asp-X-X-His motif in their active sites. The similarity extends beyond the structures of the active sites and

includes the tertiary folds of the active domain of each protein, as well as a common proposed reaction mechanism. This close relationship that exists between MMO and RNR suggests an evolutionary connection and enables us to discuss both proteins in a comparative manner.

Soluble MMO produced by methanotrophic bacteria catalyzes the hydroxylation of methane, which requires cleavage of the stable and non-polar C–H bond in methane [78]. The MMO enzyme consists of three components: a hydroxylase protein (MMOH), a regulatory protein for molecular oxygen binding, called component B (MMOB), and a reductase (MMOR), which is a 2Fe2S protein that provides two electrons to the hydroxylase. The reaction cycle of MMOH with methane or other alkanes can be summarized by the following set of reactions.

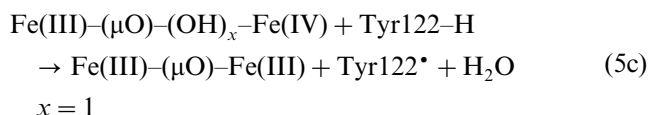
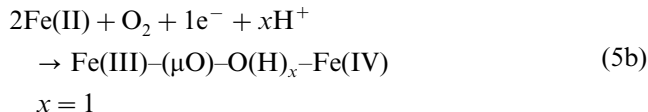
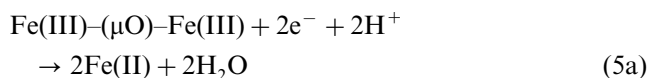


where R is methyl or higher alkyl groups. This simple sequence of reaction steps belies the structural and energetic complexities associated with the catalytic process.

In addition to hydroxylation, other reactions are catalyzed by this enzyme, including epoxidation, dehalogenation, and in some cases, desaturation (which also occurs in the related binuclear non-heme iron protein, stearoyl-ACP Δ^9 desaturase). As methanotrophic bacteria intercept and convert nearly 1 billion tons of methane annually [79] MMO is important in the global regulation of methane (a potent greenhouse gas). Also, due to their ability to react with many hydrocarbons, in particular trichloroethylene, a toxic and carcinogenic pollutant in groundwater, methanotrophs have been

used for bioremediation of toxic oil spills. The conversion of methane to methanol would facilitate transport of this fuel and chemical feedstock, but currently no efficient process on a large scale for methane hydroxylation using molecular oxygen exists [80]. A better understanding of the biological mechanism may yield improved industrial processes.

The related non-heme iron protein to MMO is Class I RNR. RNR catalyzes the reduction of ribonucleotides (NDPs) to deoxyribonucleotides (dNDPs), which is the first required step in DNA biosynthesis [81,82]. Class I RNR contains two different subunits: the first, denoted R2, contains the diiron complex which upon two-electron reduction and reaction with molecular oxygen generates a tyrosine radical (Tyr122[•]) necessary for the chemical function. Tyr122[•] serves as a ‘pilot light’ for the subsequent catalytic chemistry. A long-range proton-coupled electron-transfer process generates a thiyl radical on a cysteine of the second, larger, R1 subunit, some 30 Å away from the Tyr122[•]. R1 binds the NDP substrate and catalyzes the dehydroxylation of the 2'-hydroxyl group of the ribose ring via initial radical abstraction of the 3'-hydrogen atom. The RNR activation cycle is summarized below.



As noted earlier, class I RNR converts NDPs to dNDPs and biosynthesis of these DNA precursor molecules plays an important regulatory role in cell multiplication. This step is, naturally, of considerable interest because of the potential for developing anti-tumor and antiviral drugs capable of inhibiting RNR function in diseased tissue.

From the simple reaction steps outlined above for MMOH and RNR, it is clear that there should be significant mechanistic elements in common over these distinct reaction paths. A very important question is why the closely-related bridged diferric-oxo center in RNR (having almost identical bridging and terminal ligands to that in MMOH) undergoes a fairly similar sequence of reaction steps, but with the entirely different outcome of generation of a tyrosine radical (Tyr122[•]). For MMO and RNR, differences in reactivity with dioxygen constitute the first ‘branch point’ for variations in the subsequent chemical reactions. The larger question is how these two difficult chemical transformations are achieved and what aspects of the protein

environments direct the chemistry down these very different paths. Typically, each Fe-oxo enzyme is well-adapted to carry out a particular class of chemical reaction, be it hydroxylation, radical generation, or desaturation but site-directed mutagenesis has shown that subtle changes in the protein environment enable some of these enzymes to veer from their natural reaction pathway and achieve alternative functionality.

A major source of appeal in the study of binuclear non-heme iron enzymes is the stark contrast in functionality of RNR and MMO. The principal question as yet unanswered revolves around the subtle differences in active site structures and/or local protein environments that are causal. Spectroscopy coupled with theoretical methods has proved very valuable in probing the more fundamental, microscopic elements of the electronic and geometric structure of the active sites [77]. Mutagenesis techniques have undertaken the equally difficult objective of understanding how the protein sequence and the underlying structure of the local macroscopic environment surrounding the diiron core regulate active site structure-reactivity relationships and have provided a wealth of information testable by theoreticians [83–87]. The theoretical approach we have used in this review can also make a valuable contribution in that it interpolates between the spectroscopic-theoretical and mutagenesis-based approaches and incorporates elements of the microscopic electronic structure of the active site with the macroscopic effects of the protein environment. The challenge of our current work is to evaluate known structures and characterize the structures of the critical intermediates for both MMOH and RNR, making valuable connections with structure, spectroscopy and energetics.

6.1. Methane monooxygenase

During enzyme turnover, coupled electron and proton addition to the resting (Fe^{III}Fe^{III}) state results in the mixed-valent (Fe^{III}Fe^{II}) and reduced (Fe^{II}Fe^{II}) states (4a). Docking of the small coupling protein with the hydroxylase accelerates the reaction of the Fe^{II}Fe^{II} state with molecular O₂ and promotes formation of a metastable intermediate O, which subsequently converts into another metastable (peroxo or superoxo) adduct, intermediate P*. Two structurally-undetermined but spectroscopically-observable intermediates called P and Q are then formed. P is suspected to be a peroxide species where both oxygen atoms are bound symmetrically between the Fe^{III}Fe^{III} sites. Q is proposed to be an unprecedented, high-valent di-μ-oxo (Fe^{IV}Fe^{IV}) species responsible for the oxidation of methane (4b). A simple catalytic cycle is summarized in Fig. 10.

After the reaction of CH₄ with intermediate Q and CH₃OH release, the enzyme returns through several other proposed intermediates, R and T, [3] to its native

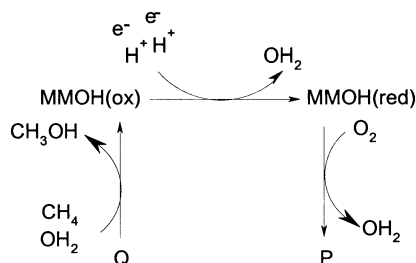


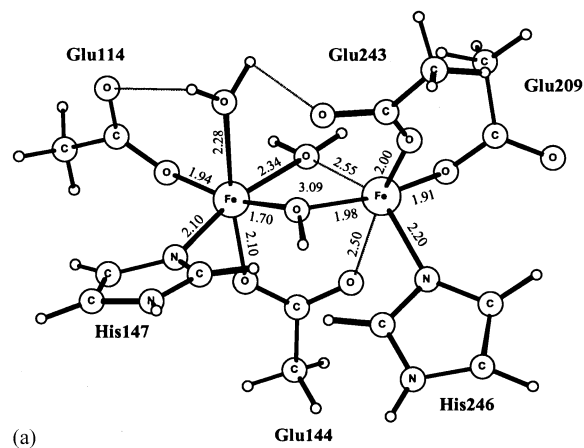
Fig. 10. Proposed simple catalytic cycle for MMO.

form (4c). Protein structures have only been solved for the oxidized $Fe^{III}Fe^{III}$, mixed-valent $Fe^{III}Fe^{II}$ and reduced $Fe^{II}Fe^{II}$ forms (Fig. 11). To validate our methodology and provide insight into the active site and protein structures, we focused our initial calculations on the oxidized $Fe^{III}Fe^{III}$ and reduced $Fe^{II}Fe^{II}$ states of the MMOH catalytic cycle for which X-ray structures are available for comparison [4,88].

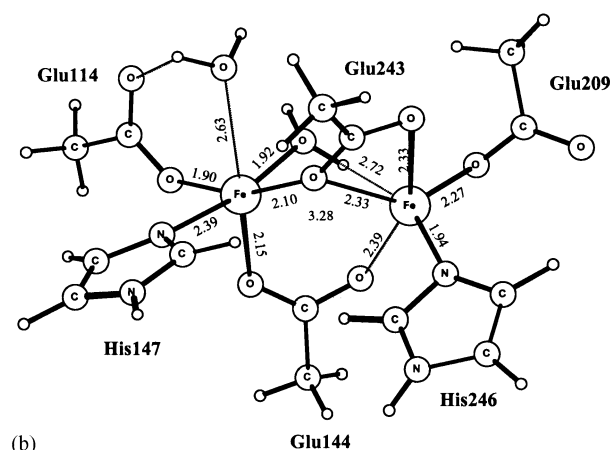
In general, calculated geometries of several model clusters are in reasonable agreement with the X-ray analyses and due to the large Fe–Fe separations, insensitive to the F or AF alignment of electron spins on adjacent Fe sites. For the more oxidized $Fe^{IV}Fe^{IV}$ and $Fe^{III}Fe^{IV}$ states where Fe–Fe separations are shorter according to EXAFS measurements, the difference in calculated geometry between the AF and F states is more pronounced. The most notable discrepancies between calculation and experiment appear in some modest reorientation of the coordinated His and Glu amino acid sidechains for both states. Typical RMSDs (calculated vs. experimental) over heavy atoms of these clusters range between 0.75 and 1.12 Å.

When cluster models are small and comprise only first shell ligands, intra-molecular pT events on the cluster occur. As the protonation state of a coordinated ligand is usually correlated with bond length, significant differences between calculated and experimental Fe^{III} –OH distances emerge. The quantum calculated bond lengths are in all cases reasonable and in agreement with Fe^{III} –OH distances observed in synthetic complexes. For model systems that include a larger portion of the local environment (including first-shell Glu243 and a pool of waters and a neutral Thr213 residue that lie close to the upper surface of the diiron cluster) the resultant energetics associated with the tautomeric forms of the oxidized $Fe^{III}Fe^{III}$ suggest a possible pathway via Thr213– H_2O –Glu238 which protons may access the active site relatively easily. Significant Fe–ligand covalency is evident from the ESP atom charges in all cases, consistent with very strong ligand \rightarrow metal charge transfer from the μOH and μ -carboxylato bridging ligands.

Even for the well-characterized oxidized $Fe^{III}Fe^{III}$ and reduced $Fe^{II}Fe^{II}$ states of MMOH, several issues remain unresolved [89]. The protein crystallography



(a)



(b)

Fig. 11. Crystal structures of the active sites of MMO in the (a) resting and (b) reduced forms.

data for the oxidized $Fe^{III}Fe^{III}$ state suggest that the solvent-derived bridging ligands differ in the two bacterial sources. This raises the question of whether the solvent ligands are water and hydroxide or two hydroxide ligands. The calculated acidity (pK_a) of the bridging water for Fig. 11(a) (pK_a in *M. trichosporium* protein = 7.7) suggests that the two possible forms are in equilibrium. A comparison of the calculated and experimental structural and magnetic data in combination with the pK_a calculations, therefore, allows the active site cluster in *M. trichosporium* to be best described as a diiron unit bridged by two hydroxide ligands having neutral net charge. This would be consistent with the energetic findings of other DFT studies that also find the two hydroxide structure to be energetically most favorable.

In the *M. capsulatus* protein, however, an exogenous acetate ion derived from the NH_4OAc buffer raises the calculated pK_a value for the bridging water to 23.9. This high pK_a in combination with the calculated structural and magnetic data suggest that the proton is effectively bound to both the acetate ion and the bridging water in a very short $AcO^{\bullet\bullet}H^{\bullet\bullet\bullet}OH$ hydrogen bond. The

equivalent acidity calculated in pure solvent ($pK_a = 13.3$) is much less than in the protein. A shift of 10 pK_a units illustrates the significance of the protein environment. Without the acetate, the calculated bridging water pK_a in *M. capsulatus* = 9.6, two pK_a units higher than calculated in *M. trichosporium*. This affects the water–hydroxide equilibrium and the effective active site charge.

6.2. Ribonucleotide reductase

Under physiological conditions, coupled electron and pT to the resting $Fe^{III}Fe^{III}$ state generates the reduced $Fe^{II}Fe^{II}$ state and X-ray structures of the protein are available to reasonable resolution for both forms (Fig. 12) (5a) [10].

Following the binding, reduction and cleavage of dioxygen by the $Fe^{II}Fe^{II}$ state, the active site acquires an extra electron from the protein matrix to give a structurally ill-characterized $Fe^{III}Fe^{IV}$ intermediate (5b), capable of abstracting an electron (and a proton) from Tyr122 to yield a neutral Tyr radical and the active $Fe^{III}Fe^{III}$ form (5c). Substrate reactions at R1 are then initiated by a complicated sequence of long-range eT over a distance of 30 Å whereby the radical character is transferred back and forth as required from Tyr122 to Cys439, the latter being the site of substrate binding and

chemical transformation. The reduction of all four NTPs then begins the process of DNA synthesis.

Our approach to studying RNR paralleled that of MMOH. Geometry optimizations of structures of the crystallographically characterized oxidized $Fe^{III}Fe^{III}$ (also called the ‘met’ form since the Tyr122 is usually in the Tyr122–OH form and not the active Tyr122 form) [90] and reduced $Fe^{II}Fe^{II}$ [91] states of the catalytic cycle were performed. Calculated geometries [92] compared very well with the known crystal data from *E. coli*. In the $Fe^{II}Fe^{II}$ structure, the calculated Fe–Fe distance of 4.1 Å is a little longer than experiment (3.9 Å) but very similar to that observed in the related stearyl–acyl-carrier protein delta-9-desaturase (Fe–Fe = 4.22 Å) [93]. Heisenberg J values measured in the protein range from -90 to -108 cm^{-1} for $Fe^{III}Fe^{III}$ [94–96] and -0.5 cm^{-1} for RNR(red) [97]. The J value calculated for $Fe^{III}Fe^{III}$ of -130 cm^{-1} is consistent with both the protein data and J values measured for model complexes that display the $Fe^{III}O_2^-Fe^{III}$ unit [98,99]. The experimental value of -0.5 cm^{-1} reported for the $Fe^{II}Fe^{II}$ state (vs. $+13$ cm^{-1} , calculated, also very small) indicates the exchange coupling is reduced relative to that in the oxidized $Fe^{III}Fe^{III}$ state. The same trend is seen in the analogous MMOH clusters over the same oxidation levels—a direct consequence of the overall reduction in charge on the Fe sites and a reduced Fe–ligand covalency. Mediated only by the $\mu_1,3$

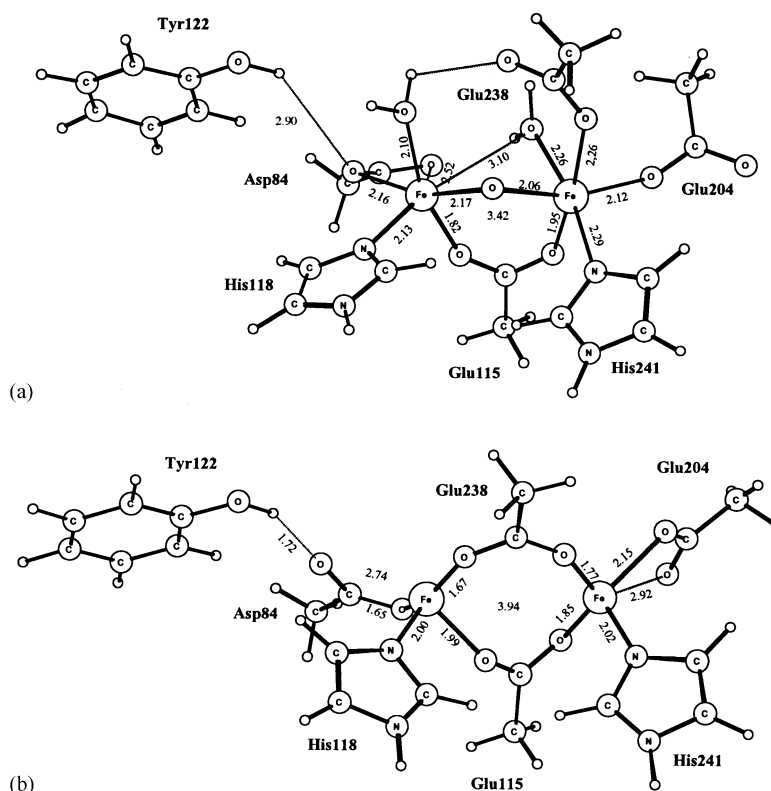


Fig. 12. Crystal structures of the active sites of RNR in the (a) resting and (b) reduced forms.

carboxylate bridges in $\text{Fe}^{\text{II}}\text{Fe}^{\text{II}}$ RNR, the coupling is thus very weak and lies close to the point at which AF to F spin alignments may interchange.

6.3. Interaction with the protein environment for structurally characterized MMOH and RNR clusters

For MMOH and RNR, enzyme function involves significant active site reorganization to several intermediates during turnover, suggesting that the active site is only weakly linked to some of the surrounding protein residues. This weak link enables the energetic transformation from one intermediate to the next. For MMOH and RNR, we have broken the total electrostatic interaction energy of the active site in the protein down into energetic contributions from the active site with the dielectric media (protein and solvent) and with the surrounding amino acid residues (screened charge–

charge), respectively [89b,92]. Large protein field interaction energies should be indicative of a significant environmental effect, perhaps large energy barriers associated with intermediate interconversion and restricting the geometric flexibility required for catalysis.

For the MMOH $\text{Fe}^{\text{III}}\text{Fe}^{\text{III}}$ state in Fig. 13(a), the size and distribution of the protein field stabilization energy (kcal mol^{-1}) indicates how the protein field anchors the active site to a base mainly composed of anionic and polar residues. Generally, Glu, Gln and Asp type sidechains appear responsible for stabilizing the active site in the protein; Arg and Lys sidechains impose a degree of destabilization. The residues highlighted may be of direct interest to those interested in probing the structure–function relationship through extensive site-directed mutagenesis studies.

Furthermore, the absence of electrostatic interactions between the protein–solvent environment and the upper

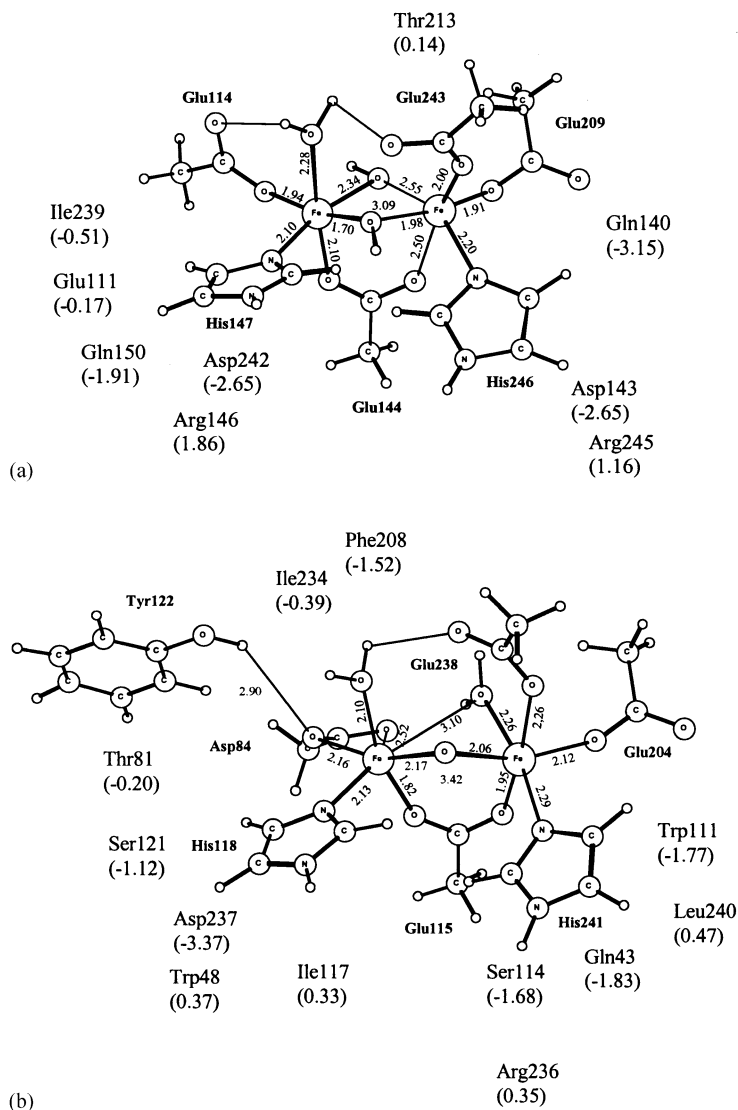


Fig. 13. Electrostatics contributions of residues in the local environment around (a) MMO and (b) RNR.

portion of the active site suggests a possible role in catalysis. The link to the protein is weaker for the top half of the cluster compared with the bottom portion, with the top containing several first-shell Glu residues surrounded by a cluster of neutral water molecules and a neutral threonine residue, while the bottom half is largely anchored to the protein. The mobility of Glu243 on the upper surface is an essential requirement for the conversion of MMOH Fe^{III}Fe^{III} into MMOH Fe^{II}Fe^{II}. The inherent flexibility associated with Glu114 and Glu209 at the active site may also be suggestive of a possible functional role during the remaining stages of the catalytic cycle, i.e. during reaction with molecular oxygen and methane and return of the enzyme to the resting form. Catalysis is thus anticipated to primarily take place on the upper surface of the active site cluster.

The overall distribution of the protein field energetics in the Fe^{III}Fe^{III} state for RNR in Fig. 13(b) bears a resemblance to that in MMOH Fe^{III}Fe^{III}. For RNR specifically [92], the lower half of the active site appears embedded in a crescent of charged and polar residues which serve to limit the mobility of the bottom portion of the diiron site (similar to MMOH Fe^{III}Fe^{III}). It is, therefore, highly unlikely that Glu115 directly participates in catalysis since surrounding residues His118 and His241 are anchored to the protein by hydrogen bonds to Asp237, Ser114 and Gln43. By contrast, the density of protein residues around the upper portion of the cluster is relatively small. Few residues appear capable of constraining the upper portion of the cluster, particularly around Tyr122, Asp84 and Glu238. This type of electrostatic picture would be consistent with experimental evidence regarding RNR function and allows us to speculate on how the cluster rearranges. We suppose that the position of Tyr122 changes in response to the needs of redox state of the diiron cluster, Asp84 is capable of using either of its O δ atoms to mediate coupled electron and pT between Tyr122 and the diiron site, and Glu238 carboxylate shifts from one coordination mode to another, switching on or off the interaction between Tyr122 and Asp84.

Generally, the RNR and MMOH active sites are found to have similar interaction energies (in terms of protein field components) [92] in the protein environments, consistent with the overall similarity in composition of active site structures and local fold of the bundle of 4 α -helices in which each active site is found in the proteins. The important residue–cluster interactions selected out by the electrostatics profiles (Fig. 13) suggest the similarity in protein field effects is due to cognate residues surrounding the active sites in both proteins. The replacement of one or several residues across a whole sequence does not appear to adversely affect the protein field energetics. In fact, both the RNR and MMOH protein structures suggest that replacement of one or several residues also does not affect the ability

of the protein to fold to its required functional form and several residues are quite easily interchangeable without loss of structural integrity. The folded form, therefore, appears as a variation on the same theme regardless of the amino-acid residues and explains the prevalence of a motif of 4 α -helices across the larger family of diiron proteins [77] and the different residue combinations found in the secondary structural elements of the proteins.

6.4. MMOH(Q)

Our initial calculations for intermediate Q of MMOH [100], the proposed high-valent Fe^{IV}Fe^{IV} species capable of oxidizing methane in the catalytic cycle of MMO, have been largely guided by the spectroscopic data [77]. Presently, no X-ray structural data exist for Q and no Fe^{IV}Fe^{IV} model complexes with biologically relevant ligands have been stabilized in aqueous solution. The identity of intermediate Q is thus, currently, an unknown quantity but a topic of much interest. Freeze–quench trapping techniques coupled with Mössbauer and EXAFS spectroscopies have provided the most insight into the structure of Q. Mössbauer data indicate that Q is a diiron cluster that exhibits diamagnetism at high magnetic field strength [101] with two near-equivalent Fe^{IV} sites that are AF coupled ($J < -30$ cm⁻¹) [102,103]. XAS experiments on *M. trichosporium* indicate pre-edge areas consistent with Fe coordination numbers of 5 or lower [79]. EXAFS spectra from *M. trichosporium* suggest a diamond core (Fe₂O₂) exists comprising one short (1.77 Å) and one long (2.06 Å) bond to each Fe and an Fe–Fe distance ranging 2.46–2.52 Å [79,104]. In attempting to construct a quantum chemical model that accurately represents intermediate Q, our working hypothesis was that the active site cluster be consistent with most of these experimental observations.

We built a large quantum model of Q containing 102 atoms (Fig. 14) that incorporates a number of second- and third-shell amino-acid residues (Asp143, Asp242, Gln140, Arg245 and Arg146). These residues appear to be structurally, electrostatically, and therefore energetically, significant from our protein field electrostatics breakdown [89b]. We have also incorporated water molecules to H-bond to oxygens of Glu residues as we anticipate water plays a key role in stabilizing the conversion of one intermediate to another, along with the carboxylate shifts. The primary goal of developing this model that complements the work of Siegbahn [105] and Dunietz et al. [106] was to evaluate how the properties of the active site are governed by the spin state ($S = 2$, HS or $S = 1$, intermediate spin (IS)) of the individual Fe sites [105] when second- and third-shell amino-acid ligands are present. Incorporating second- and third-shell residues means the main long-range

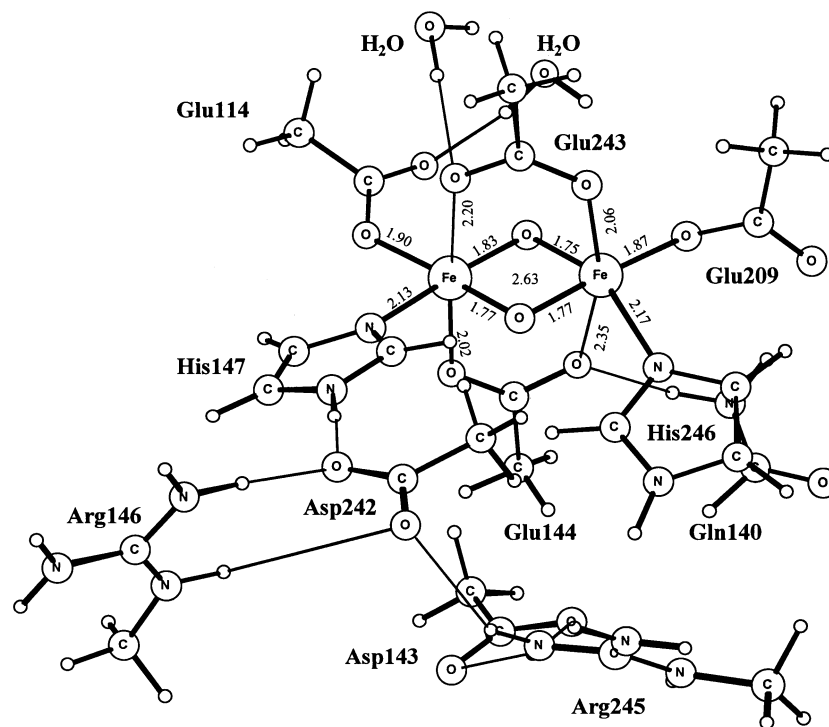


Fig. 14. Geometry optimized structure of a proposed model for intermediate Q of MMO.

protein and solvent environment effects are kept within the quantum mechanics. The characteristic features of Q guiding evaluation of the calculations include the geometry (Fe–Fe distance) and Fe coordination number, Fe net spin populations, relative energies between spin states, the exchange coupling between the two Fe sites and the spectroscopically-observed Mössbauer isomer shifts and quadrupole splittings.

Our best structural model of Q displays two strongly AF-coupled ($J_{\text{calc}} = -376 \text{ cm}^{-1}$) five-coordinate HS Fe sites separated by 2.63 Å with a small asymmetry in the Fe–O distances. While the properties of this cluster are consistent with Mössbauer and XAS spectroscopy [104], the calculated Fe–Fe distance is longer than the EXAFS-derived range (2.46–2.52 Å). EXAFS is often quite accurate for Fe–ligand and Fe–Fe distances; however, errors up to 0.2 Å compared with subsequent X-ray structures have been found for Fe–Fe distances in some cases [104]. An excited state in which two IS, six-coordinate, AF-coupled ($J = -118 \text{ cm}^{-1}$), asymmetrically-bridged Fe sites are separated by 2.42 Å lies +7.5 kcal mol⁻¹ higher in energy and +11 kcal mol⁻¹ higher after spin-projection corrections to the energies [27,107]. The presence of HS metal ions and a very short Fe–Fe separation as well as substantial asymmetry in the Fe–O bond lengths (from EXAFS) are thus mutually incompatible from our calculations [100]. The values of J calculated are, however, in reasonable accord, both in sign and magnitude, with the estimation from Mössbauer spectroscopy ($J < -30 \text{ cm}^{-1}$) [3] and that

calculated by Dunietz et al. ($J = -143 \text{ cm}^{-1}$) [106]. More extensive studies in the protein on the properties of alternative electronic states will prove extremely useful.

6.5. RNR(X)

For RNR, no complex corresponding to intermediate Q of MMOH has yet been observed. Instead, during the formation of active R2, a short-lived intermediate (X) is formed prior to formation of the tyrosyl radical [108–111]. It is of great importance to elucidate the chemical nature and structure of X because it is the key species that oxidizes tyrosine to the stable radical form. Though much effort has been made to create a detailed picture of X, its precise structure is still a topic of much debate. Experimental data have provided significant insight into the structure of X and it has been spectroscopically characterized as an $S = 1/2$ spin-coupled Fe^{IV}Fe^{III} system with no ligand radical character, but displaying significant spin delocalization onto the oxygen ligand(s) [112]. Initial ¹⁷O-ENDOR measurements suggest X comprises three exogenous O atoms, two of which derive from oxygen, the third coming from water [113]. ¹H-ENDOR indicates the existence of strongly-coupled, exchangeable proton(s), such that X probably has at least one hydroxo bridge [113]. Additional ¹H-ENDOR data on the R2-Y122F/Y356F mutant suggests the presence of a bridging hydroxide or a strongly-bound terminal hydroxide, but no terminally-bound

water [114]. CW and pulsed Q-band $^{1,2}\text{H}$ -ENDOR measurements, however, show the exchangeable proton signals displayed by intermediate X belong to two protons associated with a terminal water bound to Fe^{III} and not to a hydroxo bridge [115]. A very short Fe–Fe distance of 2.5 Å for X was identified by EXAFS appears in both wild-type and mutant Y122F proteins [116]. The accumulation of data has led to a proposed structure for X [117] (from CW and pulsed Q-band ^{17}O -ENDOR experiments and the ENDOR [115] and EXAFS [116]) which contains two oxygen atoms, both of which are initially derived from dioxygen. One oxygen appears as a μ -oxo bridge and one as a terminal aqua ligand (hydroxyl or water). The overall structure is proposed to contain a single oxo bridge, one terminal aqua ligand bound to the Fe^{IV} , and one or two additional monodentate oxygen bridges provided by the carboxylate oxygens of Glu115 and Glu238. On the basis of the 2.5 Å Fe–Fe distance from EXAFS, several possible core structures for X have been put forward [104,116] all of which support the existence of at least one μ -oxo bridge as part of the central core. Other possible bridging elements may also include another μ -oxo, hydroxide and monodentate or/and bidentate carboxylate group(s). Since the proposed structures for X have only one bridging μ -oxo species, it is quite different from the diamond core structure suggested previously for compound Q of MMOH. In fact, it is difficult to imagine that without the presence of two bridging carboxylates that a structure for X could obtain display an Fe–Fe distance of 2.5 Å. A bidentate carboxylate bridge is known to shorten the metal–metal distance of an $\text{Mn}_2(\mu\text{O})_2$ core by 0.1 Å [104] while two bidentate carboxylate bridges contract the metal–metal separation in a $\text{Fe}_2(\mu\text{OH})_2$ complex by at least 0.2 Å [104,118]. Since Glu115 and Glu238 appear as μ -1,3 bidentate bridging in the active site of the $\text{Fe}^{\text{II}}\text{Fe}^{\text{II}}$ state (Fig. 12), a similar coordination mode has been proposed in X to attain the 2.5 Å distance [104,119,120].

Even with all the above experimental data, the structure of X is still unknown and from a theoretical perspective, X received much less attention than intermediate Q of MMOH. With the EXAFS measurement acting as a guide, recent B3LYP DFT calculations on a model for intermediate X used a model containing two bridging carboxylates [119,120]. The calculated Fe–Fe distance of 2.61 Å closely resembled the EXAFS measurement and was only 0.07 Å longer than for compound Q of MMOH at the same level of treatment. The experimental data, however, are quite clear; the Fe sites must be HS Fe^{III} and Fe^{IV} . The calculated spin densities from the calculations for the Fe^{III} and Fe^{IV} sites of X were $s = 0.99$ and 1.71, respectively, suggestive that in fact, a LS $S = 1/2$ Fe^{III} site was AF coupled to an intermediate spin $S = 1$ Fe^{IV} site to give a cluster of total spin $S = 1/2$. This last point merely serves to highlight

the difficulties in obtaining the correct spin state of the cluster when several possibilities for states that lie close in energy exist.

6.6. Summary

In this section, we have presented some of the results of electronic structure calculations, both ours and others, on well-defined iron-oxo dimer complexes containing bridging aquo, hydroxo, oxo, and carboxylate groups. Our methodology appears valid in that the calculated structures and properties of the cluster models we have tested appear to be in reasonable accord with the experimental data for synthetic iron-oxo systems and the enzyme active sites for which structures are available. In terms of our work, the challenge is to improve our understanding of, and create and refine the structures of, the critical intermediates for both MMO and RNR, making connections with structure, spectroscopy, and energetics. This will enable us to further develop a deeper understanding of the reaction pathways and intermediate interconversion in the context of the dynamic protein–solvent environment.

7. Conclusions

We have examined aspects of redox energetics and reaction pathways for some selected metalloenzymes. Often changes in ligand coordination accompany redox or protonation events. eT, pT, and H atom transfer events are common within the transition metal active site and do not always involve the substrate directly (for example, in galactose oxidase, Scheme 1 and in MMO, Fig. 10, and for Fe,MnSODs). eT and oxygen species (O_2 , O_2^-) binding are important driving forces through the catalytic cycle (for Mn,FeSOD, galactose oxidase, MMO, and RNR). Charged H-bond networks both can provide stable platforms for the active site, and facilitate reactions (as for MMO and RNR). This intimate coordinated dance of electron and pT with oxygen binding and reduction allows for efficient catalytic processes with low reaction barriers (Scheme 1 and Fig. 5 for galactose oxidase, Fig. 10 for MMO). There are many gaps in our understanding of energetics of these reaction pathways, as well as in their specificity and selectivity. In addition to finding improved theoretical/computational tools for these problems, there is a need also for chemical insights to systematize the molecular logic of metalloenzyme structure and function.

Acknowledgements

We thank NIH for financial support (GM43278 to L.N.). F.H. thanks the Wenner–Gren Foundation for financial support. We thank D. Bashford and his group (V. Dillet, V. Spassov, D. Asthagiri) for their contributions to the electrostatics work, and D. Case, J. Li for contributions to both methodology and applications.

References

- [1] J.J.R. Frausto da Silva, R.J.P. Williams, *The Biological Chemistry of the Elements*, Clarendon Press, Oxford, 1991.
- [2] B.K. Burgess, D.J. Lowe, *Chem. Rev.* 96 (1996) 2983.
- [3] B.J. Wallar, J.D. Lipscomb, *Chem. Rev.* 96 (1996) 2625.
- [4] N. Elango, R. Radhakrishnan, W.A. Froland, B.J. Wallar, C.A. Earhart, J.D. Lipscomb, D. Ohlendorf, *Protein Sci.* 6 (1997) 556.
- [5] P. Richard, A. Ehrenberg, *Science* 221 (1983) 514.
- [6] M.S. Lah, M.M. Dixon, K.A. Patridge, W.C. Stallings, J.A. Fee, M.L. Ludwig, *Biochemistry* 34 (1995) 1646.
- [7] A.F. Miller, D.L. Sorkin, *Comments Mol. Cell. Biophys.* 9 (1997) 1.
- [8] J.M. Castagnetto, S.W. Hennessy, V.A. Roberts, E.D. Getzoff, J.A. Tainer, M.E. Pique, *Nucleic Acids Res.* 30 (2002) 379.
- [9] M.L. Ludwig, A.L. Metzger, K.A. Patridge, W.C. Stallings, *J. Mol. Biol.* 219 (1991) 335.
- [10] J.-A. Stubbe, W.A. van der Donk, *Chem. Rev.* 98 (1998) 705.
- [11] D.L. Vander Jagt, in: D. Dolphin, R. Poulson, O. Avramovic (Eds.), *Coenzymes and Cofactors*, vol. 3A, Wiley, New York, 1989, pp. 597–641.
- [12] L. Que, Jr., Y. Dong, *Acc. Chem. Res.* 29 (1996) 190.
- [13] R.H. Holm, P. Kennepohl, E.I. Solomon, *Chem. Rev.* 96 (1996) 2239.
- [14] A.M. Valentine, S.J. Lippard, *J. Chem. Soc. Dalton Trans.* (1997) 3925.
- [15] J.W. Whittaker, M.M. Whittaker, *J. Am. Chem. Soc.* 113 (1991) 5528.
- [16] H. Beinert, R.H. Holm, E. Munck, *Science* 277 (1997) 653.
- [17] A. Mondragon, E.C. Griffith, L. Sun, F. Xiong, C. Armstrong, J.O. Liu, *Biochemistry* 36 (1997) 4934.
- [18] N.L. Ogihara, H.E. Parge, P.J. Hart, M.S. Weiss, J.J. Goto, B.R. Crane, J. Tsang, K. Slater, J.A. Roe, J.S. Valentine, D. Eisenberg, J.A. Tainer, *Biochemistry* 35 (1996) 2316.
- [19] S.J. Lippard, J.M. Berg, *Principles of Bioinorganic Chemistry*, University Science Books, Mill Valley, CA, 1994.
- [20] A.D. Becke, in: D.R. Salahub, M.C. Zerner (Eds.), *The Challenge of d and f Electrons*, American Chemical Society, Washington, DC, 1989, pp. 165–179.
- [21] J.P. Perdew, *Phys. Rev. B* 33 (1986) 8822.
- [22] J.P. Perdew, *Phys. Rev. B* 34 (1986) 7406.
- [23] A.D. Becke, *J. Chem. Phys.* 98 (1993) 5648.
- [24] W. Kohn, A.D. Becke, R.G. Parr, *J. Phys. Chem.* 100 (1996) 12974.
- [25] A. Becke, *J. Chem. Phys.* 97 (1992) 9173.
- [26] L. Noodleman, T. Lovell, T. Liu, F. Himo, R.A. Torres, *Curr. Opin. Chem. Biol.* 6 (2002) 259.
- [27] L. Noodleman, *J. Chem. Phys.* 74 (1981) 5737.
- [28] L. Noodleman, E.J. Baerends, *J. Am. Chem. Soc.* 106 (1984) 2316.
- [29] L. Noodleman, C.Y. Peng, D.A. Case, J.-M. Mouesca, *Coord. Chem. Rev.* 144 (1995) 199.
- [30] J. Li, L. Noodleman, in: E.I. Solomon, K.O. Hodgson (Eds.), *ACS Symposium Series 692: Spectroscopic Methods in Bioinorganic Chemistry*, American Chemical Society, Washington, DC, 1998, pp. 179–197.
- [31] T.C. Brunold, E.I. Solomon, *J. Am. Chem. Soc.* 121 (1999) 8277.
- [32] T.C. Brunold, E.I. Solomon, *J. Am. Chem. Soc.* 121 (1999) 8288.
- [33] T. Lovell, W.-G. Han, T. Liu, L. Noodleman, *J. Am. Chem. Soc.* 124 (2002) 5890.
- [34] C.M. Wilmot, A.R. Pearson, *Curr. Opin. Chem. Biol.* 6 (2002) 202.
- [35] J. Li, C.L. Fisher, R. Konecny, D. Bashford, L. Noodleman, *Inorg. Chem.* 38 (1999) 929.
- [36] M.W. Whittaker, J.W. Whittaker, *J. Biol. Inorg. Chem.* 2 (1997) 667.
- [37] B.R. Crane, L.M. Siegel, E.D. Getzoff, *Science* 270 (1995) 59.
- [38] J. Li, M.R. Nelson, C.Y. Peng, D. Bashford, L. Noodleman, *J. Phys. Chem. A* 102 (1998) 6311.
- [39] R. Konecny, J. Li, C.L. Fisher, V. Dillet, D. Bashford, L. Noodleman, *Inorg. Chem.* 38 (1999) 940.
- [40] D. Bashford, *Scientific Computing in Object Oriented Parallel Environments (Lecture Notes in Computer Science) ISCOPE97*, Springer, Berlin, 1997, pp. 233–240.
- [41] D. Bashford, *Curr. Opin. Struct. Biol.* 1 (1991) 175.
- [42] D. Sitkoff, K.A. Sharp, B. Honig, *J. Phys. Chem.* 98 (1994) 1978.
- [43] D.A. Pearlman, D.A. Case, J.C. Caldwell, W.R. Ross, III, T.E. Cheatham, S. Debolt, D. Ferguson, G. Seibel, P. Kollman, *Comp. Phys. Commun.* 91 (1995) 1.
- [44] M.V. Botuyan, A. Toy-Palmer, J. Chung, R.C. Blake, II, P. Beroza, D.A. Case, H.J. Dyson, *J. Mol. Biol.* 263 (1996) 752.
- [45] G.M. Ullmann, L. Noodleman, D.A. Case, *J. Biol. Inorg. Chem.* 7 (2002) 632.
- [46] C.M. Breneman, K.B. Wiberg, *J. Comp. Chem.* 11 (1990) 361.
- [47] J.-M. Mouesca, J.L. Chen, L. Noodleman, D. Bashford, D.A. Case, *J. Am. Chem. Soc.* 116 (1994) 11898.
- [48] D. Bashford, K. Gerwert, *J. Mol. Biol.* 224 (1992) 473.
- [49] J. Li, C.L. Fisher, J.L. Chen, D. Bashford, L. Noodleman, *Inorg. Chem.* 35 (1996) 4694.
- [50] J.L. Chen, L. Noodleman, D.A. Case, D. Bashford, *J. Phys. Chem.* 98 (1994) 11059.
- [51] W.H. Richardson, C.Y. Peng, D. Bashford, L. Noodleman, D.A. Case, *Int. J. Quantum Chem.* 61 (1997) 207.
- [52] T. Simonson, G. Archontis, M. Karplus, *J. Phys. Chem. B* 103 (1999) 6142.
- [53] G.E.O. Borgstahl, H.E. Parge, M.J. Hickey, W.F. Breyer, Jr., R.A. Halliwell, J.A. Tainer, *Cell* 71 (1992) 107.
- [54] W.-G. Han, T. Lovell, L. Noodleman, *Inorg. Chem.* 41 (2002) 205.
- [55] J. Hsu, Y. Hsieh, C. Tu, D. O'Connor, H.S. Nick, D.N. Silverman, *J. Biol. Chem.* 271 (1996) 17687.
- [56] Y. Guan, M.J. Hickey, G.E.O. Borgstahl, R.A. Hallewell, J.R. Lepock, D. O'Connor, Y. Hsieh, H.S. Nick, D.N. Silverman, J.A. Tainer, *Biochemistry* 37 (1998) 4722.
- [57] Y. Hsieh, Y. Guan, C. Tu, P.J. Bratt, A. Angerhofer, J.R. Lepock, M.J. Hickey, J.A. Tainer, H.S. Nick, D.N. Silverman, *Biochemistry* 37 (1998) 4731.
- [58] S.D. Zaric, D.M. Popovic, E.-W. Knapp, *Chem. Eur. J.* 6 (2000) 3935.
- [59] J.W. Whittaker, *J. Phys. Chem. B* 101 (1997) 674.
- [60] E. Yiklimaz, J. Xie, T.C. Brunold, A.-F. Miller, *J. Am. Chem. Soc.* 124 (2002) 3482.
- [61] (a) J.P. Klinman, *Chem. Rev.* 96 (1996) 2541;
(b) J.W. Whittaker, in: H. Sigel, A. Sigel (Eds.), *Metal Ions in Biological Systems, Metalloenzymes Involving Amino Acid-Residue and Related Radicals*, vol. 30, Marcel Dekker, New York, 1994, p. 315.
- [62] N. Ito, S.E.V. Phillips, C. Stevens, Z.B. Ogel, M.J. McPherson, J.N. Keen, K.D.S. Yadav, P.F. Knowles, *Nature* 350 (1991) 87.
- [63] (a) M.M. Whittaker, J.W. Whittaker, *J. Biol. Chem.* 263 (1988) 6074;

- (b) B.P. Branchaud, M.P. Montague-Smith, D.J. Kosman, F.R. McLaren, *J. Am. Chem. Soc.* 115 (1993) 798;
- (c) M.M. Whittaker, J.W. Whittaker, *Biophys. J.* 64 (1993) 762.
- [64] (a) R.M. Wachter, B.P. Branchaud, *J. Am. Chem. Soc.* 118 (1996) 2782;
- (b) R.M. Wachter, B.P. Branchaud, *Biochemistry* 35 (1996) 14425;
- (c) R.M. Wachter, M.P. Montague-Smith, B.P. Branchaud, *J. Am. Chem. Soc.* 119 (1997) 7743.
- [65] F. Himo, L.A. Eriksson, F. Maseras, P.E.M. Siegbahn, *J. Am. Chem. Soc.* 122 (2000) 8031.
- [66] (a) F. Maseras, K. Morokuma, *J. Comp. Chem.* 16 (1995) 1170;
- (b) F. Maseras, *Top. Organomet. Chem.* 4 (1999) 165;
- (c) G. Ujaque, F. Maseras, A. Lledos, *J. Am. Chem. Soc.* 121 (1999) 1317;
- (d) F. Maseras, O. Eisenstein, *New J. Chem.* 22 (1998) 5.
- [67] (a) Y. Wang, T.D.P. Stack, *J. Am. Chem. Soc.* 118 (1996) 13097;
- (b) Y. Wang, J.L. DuBois, B. Hedman, K.O. Hodgson, T.D.P. Stack, *Science* 279 (1998) 537.
- [68] U. Rothlisberger, P. Carloni, *Int. J. Quant. Chem.* 73 (1999) 209.
- [69] R.M. Wachter, B.P. Branchaud, *Biochim. Biophys. Acta* 1384 (1998) 43.
- [70] S. Itoh, K. Hirano, A. Furuta, M. Komatsu, Y. Ohshiro, A. Ishida, S. Takamuku, T. Kohzuma, N. Nakamura, S. Suzuki, *Chem. Lett.* (1993), 2099.
- [71] (a) B. Mannervik, in: W.B. Jakoby (Ed.), *Enzymatic Basis of Detoxification*, vol. 2, Academic Press, New York, 1980, pp. 263–273;
- (b) P.J. Thornalley, *Biochem. J.* 269 (1990) 1.
- [72] (a) P.J. Thornalley, *Chem.-Biol. Interact.* 111–112 (1998) 137;
- (b) J.F. Bernard, D.L. Vander Jagt, J.F. Honek, *Biochim. Biophys. Acta* 1208 (1994) 127;
- (c) M.J. Kavarana, E.G. Kovaleva, D.J. Creighton, M.B. Wollman, J.L. Eiseman, *J. Med. Chem.* 42 (1999) 221.
- [73] (a) B. Mannervik, L. Lindström, T. Bartfai, *Eur. J. Biochem.* 29 (1972) 276;
- (b) L. Uotila, M. Koivusalo, *Eur. J. Biochem.* 52 (1975) 493.
- [74] A.D. Cameron, M. Ridderström, B. Olin, M.J. Kavarana, D.J. Creighton, B. Mannervik, *Biochemistry* 38 (1999) 13480.
- [75] J.A. Landro, E.J. Brush, J.W. Kozarich, *Biochemistry* 31 (1992) 6069.
- [76] F. Himo, P.E.M. Siegbahn, *J. Am. Chem. Soc.* 123 (2001) 10280.
- [77] E.I. Solomon, T.C. Brunold, M.I. Davis, J.N. Kemsley, S.-K. Lee, N. Lehnert, F. Neese, A.J. Skulan, Y.-S. Yang, J. Zhou, *Chem. Rev.* 100 (2000) 235.
- [78] Y. Jin, J.D. Lipscomb, *J. Biol. Inorg. Chem.* 7 (2001) 717.
- [79] L. Shu, J.V. Nesheim, K. Kauffmann, E. Münck, J.D. Lipscomb, L. Que, Jr., *Science* 275 (1997) 515.
- [80] A.C. Rosenzweig, H. Brandstetter, D.A. Whittington, P. Nordlund, S.J. Lippard, C.A. Frederick, *Proteins: Struct. Funct. Gene* 29 (1997) 141.
- [81] R.C. Prince, *TIBS* 13 (1988) 286.
- [82] P. Nordlund, B.-M. Sjöberg, H. Eklund, *Nature* 345 (1990) 593.
- [83] W.C. Voegtli, N. Khidekel, J. Baldwin, B.A. Ley, J.M. Bollinger, A.C. Rosenzweig, Jr., *J. Am. Chem. Soc.* 122 (2000) 3255.
- [84] M.E. Andersson, M. Hogbom, A. Rinaldo-Matthis, K.K. Andersson, B.-M. Sjöberg, P. Nordlund, *J. Am. Chem. Soc.* 121 (1999) 2346.
- [85] W. Tong, S. Chen, S.G. Lloyd, D.E. Edmondson, B.H. Huynh, J. Stubbe, S. Han, A. Arvai, J. Tainer, *Biochemistry* 37 (1998) 5840.
- [86] S.E. Parkin, S. Chen, B.A. Ley, L. Mangravite, D.E. Edmondson, B.H. Huynh, J.M. Bollinger, Jr., *Biochemistry* 37 (1998) 1124.
- [87] J. Baldwin, P. Moenne-Loccoz, C. Krebs, B.A. Ley, D.E. Edmondson, B.H. Huynh, T.M. Loehr, J.M. Bollinger, Jr., *J. Inorg. Biochem.* 74 (1999) 74.
- [88] A.C. Rosenzweig, P. Nordlund, P.M. Takahara, C.A. Frederick, S.J. Lippard, *Chem. Biol.* 2 (1995) 409.
- [89] (a) T. Lovell, J. Li, L. Noodleman, *Inorg. Chem.* 40 (2001) 5251;
- (b) T. Lovell, J. Li, L. Noodleman, *Inorg. Chem.* 40 (2001) 5267.
- [90] P. Nordlund, H. Eklund, *J. Mol. Biol.* 232 (1993) 123.
- [91] D.T. Logan, X.-D. Su, A. Aberg, K. Regnstrom, J. Hajdu, H. Eklund, P. Nordlund, *Structure* 4 (1996) 1053.
- [92] T. Lovell, J. Li, L. Noodleman, *J. Biol. Inorg. Chem.* 7 (2002) 799.
- [93] Y. Lindqvist, W. Huang, G. Schneider, J. Shanklin, *EMBO J.* 15 (1996) 4081.
- [94] L. Petersson, A. Graslund, A. Ehrenberg, B.-M. Sjöberg, P. Reichard, *J. Biol. Chem.* 255 (1980) 6706.
- [95] M. Atta, C. Sheer, P.H. Fries, M. Fontecave, J.-M. Latour, *Angew. Chem. Int. Ed. Engl.* 31 (1992) 1513.
- [96] C. Galli, M. Atta, K.K. Andersson, A. Graslund, G.W. Brudvig, *J. Am. Chem. Soc.* 117 (1995) 740.
- [97] S.C. Pulver, W.H. Tong, J.M. Bollinger, Jr., J. Stubbe, E.I. Solomon, *J. Am. Chem. Soc.* 117 (1995) 12664.
- [98] H. Weihe, H.U. Gudel, *J. Am. Chem. Soc.* 119 (1997) 6539.
- [99] S.M. Gorun, S.J. Lippard, *Inorg. Chem.* 30 (1991) 1625.
- [100] T. Lovell, W.-G. Han, L. Noodleman, *J. Am. Chem. Soc.* 124 (2002) 5890.
- [101] K.E. Liu, A.M. Valentine, D. Wang, B.H. Huynh, D.E. Edmondson, A. Salifoglou, S.J. Lippard, *J. Am. Chem. Soc.* 117 (1995) 10174.
- [102] K.E. Liu, D.L. Wang, B.H. Huynh, D.E. Edmondson, A. Salifoglou, S.J. Lippard, *J. Am. Chem. Soc.* 116 (1994) 7465.
- [103] S.-K. Lee, B.G. Fox, W.A. Froland, J.D. Lipscomb, E. Münck, *J. Am. Chem. Soc.* 115 (1993) 6450.
- [104] H.F. Hsu, Y. Dong, L. Shu, Jr., V.G. Young, L. Que, Jr., *J. Am. Chem. Soc.* 121 (1999) 5230.
- [105] P.E.M. Siegbahn, *J. Biol. Inorg. Chem.* 6 (2001) 27.
- [106] B.D. Dunietz, M.D. Beachy, Y. Cao, D.A. Whittington, S.J. Lippard, R.A. Friesner, *J. Am. Chem. Soc.* 122 (2000) 2828.
- [107] J.E. McGrady, R. Stranger, T. Lovell, *J. Phys. Chem. A* 101 (1997) 6265.
- [108] J.M. Bollinger, Jr., D.E. Edmondson, B.H. Huynh, J. Filley, J.R. Norton, J. Stubbe, *Science* 253 (1991) 292.
- [109] J.M. Bollinger, Jr., J. Stubbe, B.H. Huynh, D.E. Edmondson, *J. Am. Chem. Soc.* 113 (1991) 6289.
- [110] N. Ravi, J.M. Bollinger, Jr., B.H. Huynh, D.E. Edmondson, J. Stubbe, *J. Am. Chem. Soc.* 116 (1994) 8007.
- [111] (a) J.M. Bollinger, Jr., W.H. Tong, N. Ravi, B.H. Huynh, D.E. Edmondson, J. Stubbe, *J. Am. Chem. Soc.* 116 (1994) 8015;
- (b) J.M. Bollinger, Jr., W.H. Tong, N. Ravi, B.H. Huynh, D.E. Edmondson, J. Stubbe, *J. Am. Chem. Soc.* 116 (1994) 8024.
- [112] B.E. Sturgeon, D. Burdi, S. Chen, B.H. Huynh, D.E. Edmondson, J. Stubbe, B.M. Hoffman, *J. Am. Chem. Soc.* 118 (1996) 7551.
- [113] D. Burdi, B.E. Sturgeon, W.H. Tong, J. Stubbe, B.M. Hoffman, *J. Am. Chem. Soc.* 118 (1996) 281.
- [114] A. Veselov, C.P. Scholes, *Inorg. Chem.* 35 (1996) 3702.
- [115] J.P. Willems, H.I. Lee, D. Burdi, P.E. Doan, J. Stubbe, B.M. Hoffman, *J. Am. Chem. Soc.* 119 (1997) 9816.
- [116] P.J. Riggs-Gelasco, L. Shu, S. Chen, D. Burdi, B.H. Huynh, L. Que, Jr., J. Stubbe, *J. Am. Chem. Soc.* 120 (1998) 849.
- [117] D. Burdi, J.P. Willems, P.J. Riggs-Gelasco, W.E. Antholine, J. Stubbe, B.M. Hoffman, *J. Am. Chem. Soc.* 120 (1998) 12910.
- [118] D. Lee, S.J. Lippard, *J. Am. Chem. Soc.* 120 (1998) 12153.
- [119] P.E.M. Siegbahn, *Inorg. Chem.* 38 (1999) 2880.
- [120] P.E.M. Siegbahn, M.R.A. Blomberg, *Annu. Rev. Phys. Chem.* 50 (1999) 221.